

**Multi-Grid-Cell Validation of Satellite Aerosol Property Retrievals in
INTEX/ITCT/ICARTT 2004**

P. B. Russell,¹ J. M. Livingston,² J. Redemann,³ B. Schmid,³ S. A. Ramirez,³ J. Eilers,¹ R. Kahn,⁴
A. Chu,⁵ L. Remer,⁵ P. K. Quinn,⁶ M. J. Rood,⁷ W. Wang⁷

Submitted to JGR-Atmospheres

31 May 2006

Corresponding author: Philip B. Russell
NASA Ames Research Center
MS 245-5
Moffett Field, CA 94035-1000
Phone: +1 650 604 5404
Fax: +1 650 604 6779
e-mail: Philip.B.Russell@nasa.gov

Affiliations:

¹ NASA Ames Research Center, MS 245-5, Moffett Field, CA 94035-1000. (e-mail:

Philip.B.Russell@nasa.gov)

² SRI International, 333 Ravenswood Avenue, Menlo Park, CA 94025. (e-mail:

jlivingston@mail.arc.nasa.gov)

³ Bay Area Environmental Research Institute, 560 3rd Street West, Sonoma, CA 95476. (e-mail:

bschmid@mail.arc.nasa.gov, jredemann@mail.arc.nasa.gov, saramirez@mail.arc.nasa.gov)

⁴ Jet Propulsion Laboratory, California Institute of Technology, Pasadena 91109-8099, CA, USA

⁵ NASA Goddard Space Flight Center, Laboratory for Atmospheres, Code 912, Greenbelt, MD 20771. (e-mail: achu@climate.gsfc.nasa.gov)

⁶ NOAA PMEL, 7600 Sand Point Way NE, Seattle, WA 98115 USA

⁷ Dept. of Civil & Environ. Eng., University of Illinois at Urbana-Champaign, Urbana, IL USA 61801-2352

Abstract. Aerosol transport off the US Northeast coast in Summer 2004 produced a wide range of aerosol types and aerosol optical depth (AOD) values, often with strong horizontal AOD gradients. In these conditions we flew the 14-channel NASA Ames Airborne Tracking Sunphotometer (AATS) on a Jetstream 31 (J31) aircraft. Legs flown at low altitude (usually ≤ 100 m ASL) provided comparisons of AATS AOD spectra to retrievals for 90 grid cells of the satellite radiometers MODIS-Terra, MODIS-Aqua, and MISR. Characterization of the retrieval environment was aided by using vertical profiles by the J31 (showing aerosol vertical structure) and, on occasion, shipboard measurements of scattering, absorption, and AOD.

AATS provides AOD at 13 wavelengths λ from 354 to 2138 nm, spanning the range of aerosol retrieval wavelengths for MODIS over ocean (466-2119 nm) and MISR (446-866 nm).

Midvisible AOD on low-altitude J31 legs in satellite grid cells ranged from 0.05 to 0.9, with gradients often in the range 0.05 to 0.13 per 10 km. When possible, we used ship measurements of humidified aerosol scattering and absorption to estimate AOD below the J31. In these cases, which had J31 altitudes 60-110 m ASL (typical of J31 low-altitude transects), estimated midvisible AOD below the J31 ranged from 0.003 to 0.013, with mean 0.009 and standard deviation 0.003.

MISR-AATS comparisons on 29 July 2004 in 8 grid cells (each ~ 17.6 km x 17.6 km) show that MISR versions 15 and 16 captured the AATS-measured AOD gradient (correlation coefficient $R^2=0.87$ to 0.92), but the MISR gradient was somewhat weaker than the AATS gradient. The large AOD (midvisible values up to ~ 0.9) and differing gradients in this case produced root-mean-square (RMS) MISR-AATS AOD differences of 0.03 to 0.21 (9 to 31%). MISR V15 Ångstrom exponent α ($= -\text{dlnAOD}/\text{dln}\lambda$) was closer to AATS than was MISR V16.

MODIS-AATS AOD comparisons on 8 overpasses using 61 grid cells (each nominally 10 km x 10 km) had $R^2 \sim 0.97$, with RMS AOD difference ~ 0.03 ($\sim 20\%$). About 87% of the MODIS AOD retrievals differed from AATS values by less than the predicted MODIS over-ocean uncertainty, $\Delta\tau = \pm 0.03 \pm 0.05\tau$. In contrast to the small MODIS-AATS differences in AOD, MODIS-AATS differences in Ångstrom exponent α were large: RMS differences for $\alpha(553, 855$

nm) were 0.28 for MODIS-Terra and 0.64 for MODIS-Aqua; RMS differences for $\alpha(855, 2119$ nm) were larger still: 0.61 for MODIS-Terra and 1.14 for MODIS-Aqua. The largest MODIS-AATS Ångstrom exponent differences were associated with small AOD values, for which MODIS AOD relative uncertainty is large. Excluding cases with $\text{AOD}(855 \text{ nm}) < 0.1$ reduced MODIS-AATS α differences substantially.

In one grid cell on 21 July 2004, smoke over cloud appeared to impair the MODIS-Aqua cloud mask, resulting in retrieved AODs that significantly exceeded AATS values. Experiments with extending MODIS retrievals into the glint mask yielded MODIS AODs consistently less than AATS AODs, especially at long wavelength, indicating that the current MODIS glint mask limits should not be reduced to the extent tried here. The sign of the AOD differences within the glint mask (MODIS AOD < AATS AOD) is consistent with ship-measured wind speeds there.

1. Introduction

In Summer 2004 the International Consortium for Atmospheric Research on Transport and Transformation [ICARTT, *Fehsenfeld et al.*, 2006] studied air quality, intercontinental transport, and radiative energy budgets in air masses moving across the US and over the Atlantic Ocean to Europe. Among other experiments, ICARTT included Phase A of the Intercontinental Chemical Transport Experiment (INTEX-A, Singh et al., 2006) and the Intercontinental Transport and Chemical Transformation (ITCT) experiment. Conditions during ICARTT included transport of a variety of aerosol types off the US Northeast coast, which produced a wide range of aerosol optical depth (AOD) values, as well as many cases of horizontal gradients in AOD over the Gulf of Maine. The aerosol types included biomass smoke transported from wildfires in Alaska and Western Canada as well as particles in urban and power plant plumes transported from nearby sources on the New England coast and more distant sources in the Ohio River Valley.

In this context, with support from INTEX-A and ITCT, the twin turboprop Jetstream 31 (J31) aircraft flew missions over the Gulf of Maine in July and August 2004. Its goal was to characterize aerosol, water vapor, cloud, and ocean surface radiative properties and effects in flights that sampled polluted and clean air masses in coordination with measurements by other

INTEX/ITCT/ICARTT platforms, including aircraft, a ship, and several satellites. Specific science objectives of the J31 included validating satellite retrievals of AOD spectra and of water vapor columns, as well as measuring aerosol effects on radiative energy fluxes. This paper reports J31 AOD measurements and compares them to AOD retrievals by three satellite sensors: the Multiangle Imaging SpectroRadiometer [MISR, *Diner et al.*, 1998; *Martonchik et al.*, 1998] on the satellite Terra and two Moderate Resolution Imaging Spectroradiometer [MODIS, *Kaufman et al.*, 1997] instruments, one each on the satellites Terra and Aqua. *Livingston et al.* [2006] report the J31 water vapor measurements and comparisons to satellites and in situ measurements. *Redemann et al.* [2006a] report the J31 measurements of aerosol effects on radiative energy fluxes. *Pilewskie et al.* [2006] report cloud properties derived from J31 measurements of visible and near-infrared reflectance in the presence of aerosols.

The MISR and MODIS sensors have been producing AOD products for over six years, and these products have been the subject of several validation papers [e.g., *Remer et al.*, 2002, 2005; *Chu et al.*, 2002, 2005; *Levy et al.*, 2003; *Livingston et al.*, 2003; *Schmid et al.*, 2003a; *Martonchik et al.*, 2004; *Abdou et al.*, 2005; *Kahn et al.*, 2005; *Redemann et al.*, 2005, 2006b). These papers have addressed both AOD and its dependence on wavelength λ , usually expressed as an Ångstrom exponent α ($=-\text{dlnAOD}/\text{dln}\lambda$). Nevertheless, there is a continuing need for ongoing validation studies for several reasons including:

- The scatter plots that are a staple of the validation studies cited above include points that fall outside the expected \pm one-sigma uncertainty. Measurement results that help reveal what causes these outliers can often lead to improved satellite retrievals, which in turn can bring more points within the expected uncertainty.
- New versions of satellite AOD products are being developed, and continuing validation measurements are required to inform and to evaluate these new versions.
- Although *Remer & Kaufman* [2006, Figure 10] show good agreement between global, monthly mean Level 3 AOD($0.55 \mu\text{m}$) from MODIS-Terra and MODIS-Aqua, several other studies have reported persistent differences among the archived products for AOD and Ångstrom exponent from MODIS-Terra, MODIS-Aqua, and MISR. For example, *Redemann et al.* [2004a,b] investigated regional maps of monthly-mean AOD as provided by the

MODIS-Terra and MISR satellite sensors for the month of April during the years 2000-2004. The comparisons showed significant differences in the geographic distribution of the Asian aerosol plume as it advected across the Pacific Ocean in any given year. This was particularly true for April 2001, when the ACE-Asia campaign [Huebert *et al.*, 2003] took place. In 2001, the longitudinally-averaged mid-visible AOD between 40°N and 50°N as derived by the two sensors differed by more than 20% (or 0.1). Two other studies [Gassó *et al.*, 2004; Anderson *et al.*, 2005] also performed analyses of the performance of MODIS-Terra during ACE-Asia by comparing the MODIS-derived AOD [Chu *et al.*, 2005], Ångström parameter and fine mode fraction to suborbital data. Those studies found generally close agreement between MODIS and the suborbital data for AOD, but much less agreement for the Ångström parameter and fine mode fraction. More recently Redemann *et al.* [2006b] found significant differences between MODIS-Terra and MODIS-Aqua Level 2 retrievals for both AOD and Ångström exponent in terms of their comparison to airborne sunphotometer measurements in April 2004 in the presence of mineral dust. Possible reasons for the above differences include differences in absolute calibration scales and in cloud screening; they are the subject of ongoing studies by the MODIS and MISR teams. Additional validation measurements are important to advancing those studies.

- As stressed by Anderson *et al.* [2005], there is a need for increased emphasis on validation of satellite-retrieved Ångström exponent, which is closely related to aerosol fine mode fraction and submicron fraction, and hence to designation of aerosols as anthropogenic vs. natural. Studies that have compared satellite and suborbital results for Ångström exponent [e.g., Levy *et al.*, 2003; Livingston *et al.*, 2003] have found significant differences in some situations. Gassó and O'Neill [2006] emphasized that aerosol fine mode fraction retrieved from AOD spectra describing a column cannot be used to distinguish whether the aerosol under observation is composed of layers each with distinctive modal features or all layers with the same modal features.
- The workhorse of most satellite AOD validation studies, sunphotometry at fixed ground sites, is not well suited to acquiring data over the open ocean or to examining the ability of satellite retrievals to provide consistent results across grid cell boundaries, to measure horizontal gradients accurately, and to perform well when aerosols are layered with different properties in different layers. Airborne sunphotometry is uniquely able to address these gaps and also to

measure AOD variability within satellite grid cells, to check for systematic AOD increases when approaching clouds, and to determine the spatial scale of such increases if they exist. Its use in well designed field studies can refine and validate the satellite retrieval algorithms and also help develop ways to combine the less detailed but more extensive satellite observations with detailed constraints on AOD, Ångstrom exponent, absorption, composition and their vertical and horizontal variability using the aircraft-acquired information.

2. Data Sources

2.1 Airborne sunphotometer

The NASA Ames Airborne Tracking Sunphotometer (AATS-14), which flew on the J31, measures transmission of the direct solar beam in 14 channels with center wavelengths ranging from 354 to 2138 nm. This wavelength range includes the aerosol retrieval wavelength range for MODIS over ocean (466-2119 nm) and for MISR (446-866 nm). AATS-14 azimuth and elevation motors, controlled by tracking-error signals derived from a quad-cell photodiode, rotate a tracking head to lock on to the solar beam and maintain detectors normal to it. On the J31 the AATS-14 tracking head was mounted outside and above the skin of the aircraft. This mounting gave an unobstructed view of the sun for most J31 orientations and most solar azimuth and elevation angles.

Each science channel in AATS-14 consists of a baffled entrance path, interference filter, photodiode detector, and integral preamplifier. The filter/detector/preamp sets are temperature controlled to avoid thermally induced calibration changes. The module that contains the science channels and the tracking photodiode is protected from the outside air by a quartz window that is exposed to the ambient air stream. In an effort to prevent window fogging or frost a foil heater is mounted on the inside surface of this window. The heater foil has a hole for each science channel and for the tracking detector, to permit the solar beam to pass through. AATS-14 is typically purged with dry nitrogen or zero air before each flight, as an additional fog or frost prevention measure.

AATS-14 samples at three Hz. Every four seconds it records data consisting of an average and standard deviation of nine samples taken during the first three of the four seconds. These data are stored together with data on instrument tracking and temperature control, aircraft location, and ambient temperature, dewpoint, and static pressure. The standard deviations of all the channels are used subsequently in a cloud-screening algorithm, as described by *Schmid et al.* [2003a,b]. Data are transmitted serially from a computer within the instrument to a remote operator station (laptop computer). The science data are then combined with previously determined radiometric calibration values to calculate and display preliminary aerosol optical depth (AOD, $\tau_p(\lambda)$) and columnar water vapor (CWV) in real time at the operator station.

Our methods for data reduction, calibration, and error analysis have been described in detail previously [*Russell et al.*, 1993a, 1993b; *Schmid and Wehrli*, 1995; *Schmid et al.*, 1996, 1998, 2001, 2003a,b]. The AATS-14 channels are chosen to permit separation of aerosol, water vapor, and ozone attenuation along the measured slant path. From these slant-path transmissions we retrieve $\tau_p(\lambda)$ in 13 narrow wavelength bands (centered at 354, 380, 453, 499, 519, 604, 675, 778, 865, 1019, 1241, 1558, and 2139 nm, with full-width-half-maximum bandwidths of 2.0, 4.6, 5.6, 5.4, 5.4, 4.9, 5.2, 4.5, 5.0, 5.1, 5.1, 4.9, and 17.3 nm, respectively) and the columnar amounts of water vapor (from the channel centered at 941 nm). For suitable conditions (basically solar zenith angle $>\sim 80^\circ$ and $\text{AOD}(600\text{ nm}) < \sim 0.04$) we can also retrieve ozone column content. For other conditions (including those in ICARTT), we use ozone column amounts from TOMS satellite retrievals. Resulting ozone-induced uncertainties in AOD are included in our error bars and are always < 0.01 at 600 nm and less at other wavelengths. Rayleigh scattering corrections use the *Bucholtz* [1995] cross sections and pressure measured on the J31.

In addition to the corrections for Rayleigh scattering and O_3 absorption, measurements in some AATS-14 channels require corrections for NO_2 , H_2O and $\text{O}_2\text{-O}_2$ absorption in order to retrieve AOD. Gas absorption cross-sections for the AATS-14 channels were computed using LBLRTM 6.01 [*Clough and Iacono*, 1995] with the CKD 2.4.1 continuum model using the HITRAN 2000 (v11.0) line-list [*Rothman et al.*, 2003] that includes an update for water vapor from April 2001. NO_2 cross-sections not included in LBLRTM 6.01 were taken from *Harder et al.* [1997]. For results in this paper NO_2 column content was assumed constant at 2×10^{15} molecules cm^{-2} ,

which corresponds to optical depths of 0.0011 and 0.0008 in the 380-nm and 453-nm channels, respectively. Optical depth due to absorption by O₂-O₂ was less than 0.0002 in every channel except 1241 nm, where the contribution was ~0.011 at sea level. For the 2138-nm channel, gas absorption due to CH₄, N₂O, and CO₂ was parameterized as a function of altitude using a 5th order polynomial fitting function to results from LBLRTM_v9.2 runs over a range of solar zenith angles and instrument altitudes. Optical depth due to H₂O absorption was negligible in all aerosol channels (that is, excluding 941 nm).

AATS was calibrated by analysis of sunrise measurements acquired at Mauna Loa Observatory (MLO), Hawaii, before the INTEX/ITCT/ICARTT deployment and also by analysis of sunset measurements acquired on 4 special J31 flights during INTEX/ITCT/ICARTT. Exoatmospheric detector voltages, V_0 , were derived using the Langley plot technique [e.g., *Russell et al.*, 1993a, 1993b; *Schmid and Wehrli*, 1995] for all channels except 941 nm, for which a modified Langley technique was employed to account for water vapor absorption [*Reagan et al.*, 1995; *Michalsky et al.*, 1995; *Schmid et al.*, 1996, 2001]. Resulting uncertainties in AOD are typically less than 0.01, and are shown by error bars on selected plots in this paper.

A potentially large source of calibration error is dirt deposited on the sunphotometer entrance window [e.g., *Livingston et al.*, 2003]. To minimize this error we cleaned the window carefully before each flight and inspected it carefully for dirt after each flight.

We derived profiles of aerosol extinction $\sigma_{ep}(\lambda)$ for many profiles by vertically differentiating the $\tau_p(\lambda)$ profiles (after discarding profiles influenced by considerable horizontal inhomogeneity or overlying clouds). Most vertical profiles were acquired in <20 minutes of flight time. Occasionally, $\tau_p(\lambda)$ decreased (increased) when the plane descended (ascended). In a horizontally homogeneous, time-invariant atmosphere, this would be impossible. However, in the real atmosphere it can occur because (1) the sunphotometer can only measure the transmittance of the sunphotometer-to-sun path, (2) that path in general passes through a horizontally inhomogeneous, time-varying atmosphere, and (3) the path and the atmosphere move with respect to each other as the aircraft moves and the wind blows. Before the sunphotometer $\tau_p(\lambda)$ profile is vertically differentiated to obtain $\sigma_{ep}(\lambda)$, it has to be smoothed (in

a non-biased manner) to eliminate increases in $\tau_p(\lambda)$ with height. In this study we first averaged the $\tau_p(\lambda)$ values over 20-m altitude bins and then used smoothed spline fits for this purpose. However, to avoid over-smoothing at altitudes that exhibit actual variations of $\tau_p(\lambda)$ we occasionally allow $\sigma_{ep}(\lambda)$ to become slightly negative. An example is shown in Section 3.3.

Because most of the errors in $\tau_p(\lambda)$ are of systematic nature, they cancel when differences (such as layer $\tau_p(\lambda)$) or differentiations ($\sigma_{ep}(\lambda)$) are used. However since the aircraft requires a finite time to fly a vertical profile which has a finite horizontal component, temporal and spatial variation of the aerosol above the aircraft will lead to uncertainties in the differentiated quantities.

2.2 Ship humidified scattering and absorption measurements

Because the J31 flew at a nonzero altitude (typically 60 to 100 m ASL) for the satellite validation measurements reported here, it is desirable to estimate the AOD below the J31. For this purpose we have used aerosol extinction values derived from measurements of aerosol scattering, absorption, scattering humidification, and relative humidity made on the NOAA RV *Ronald H. Brown* during times when the J31 flew by the ship and AATS could view the sun.

Aerosol scattering coefficients were measured with an integrating nephelometer at wavelengths 450, 550, and 700 nm, all at instrument relative humidity (RH) ~60%. The nephelometer had a 1.0 μm cut off diameter at 60% RH. Measured scattering coefficients were corrected for truncation errors and non-lambertian illumination using the method of Anderson and Ogren [1998]. Absorption coefficients were measured with a filter-based particle soot absorption photometer at 467, 530, and 600 nm. Calculated Angstrom exponents were used to adjust the absorption coefficients to the nephelometer wavelengths. Scattering, absorption, and ambient RH were measured with a 1 minute time resolution. At a slower resolution of ~1 hour, measurements of the dependence of aerosol scattering σ_{sp} on RH were made using one dry and one RH-scanning nephelometer [Carrico *et al.*, 2003; Wang *et al.*, 2006] with an inlet cutoff to

admit particles with diameters $<1 \mu\text{m}$ at 60% RH. The dry nephelometer measured scattering at $RH_{\text{ref}} = 26 \pm 4\%$, and the scanning nephelometer at increasing and decreasing RH up to 85%.

From the scanning and dry nephelometers we calculated the parameter γ defined by

$$f(RH, RH_{\text{ref}}) = \frac{\sigma_{\text{sp}}(RH)}{\sigma_{\text{sp}}(RH_{\text{ref}})} = \left(\frac{100\% - RH}{100\% - RH_{\text{ref}}} \right)^{-\gamma} \quad (1)$$

as

$$\gamma = \ln(f(85\%, 26\%)) / \ln[(100\% - RH_{\text{ref}}) / (100\% - RH)] \quad (2)$$

where $f(85\%, 26\%)$ values are archived in the ship data set, $RH_{\text{ref}} = 26\%$, and $RH = 85\%$. We used the archived $f(85\%, 26\%)$ values for scans with decreasing RH since we wanted to use the resulting γ values to restore the nephelometer values measured at 60% RH to the larger ambient RH values at the altitude of the inlet to the nephelometers (18 m ASL).

We interpolated the resulting γ values to the ~ 1 -minute resolution of the 60% RH nephelometer measurements, and calculated $f(RH_{\text{amb}}, RH_{\text{neph}})$ as

$$f(RH_{\text{amb}}, RH_{\text{neph}}) = \frac{\sigma_{\text{sp}}(RH_{\text{amb}})}{\sigma_{\text{sp}}(RH_{\text{neph}})} = \left(\frac{100 - RH_{\text{amb}}}{100 - RH_{\text{neph}}} \right)^{-\gamma}, \quad (3)$$

where $RH_{\text{neph}} = 60\%$, and RH_{amb} is the ambient RH. We then obtained ambient scattering as

$$\sigma_{\text{sp}}(RH_{\text{amb}}) = f(RH_{\text{amb}}, RH_{\text{neph}}) \sigma_{\text{sp}}(RH_{\text{neph}}). \quad (4)$$

We estimated ambient extinction as

$$\sigma_{ep}(RH_{amb}) = \sigma_{sp}(RH_{amb}) + \sigma_{ap}(60\%), \quad (5)$$

using the common assumption that absorption σ_{ap} is only weakly dependent on RH and can be approximated by its value at 60% RH [e.g., *Redemann et al.*, 2001].

We then estimated AOD below the J31 as

$$AOD_{belowJ31} = \sigma_{ep}(RH_{amb})z_{J31}, \quad (6)$$

where z_{J31} is the J31 altitude (typically 60 to 100 m ASL in the low-altitude passes of the Ron Brown and in the transects used for satellite validation). This approach neglects any RH_{amb} and aerosol variations with altitude below z_{J31} . Results are shown in Section 3.1, where we also note that, on the three occasions where radiosonde vertical profiles of RH_{amb} were available, using altitude-dependent RH_{amb} in place of the values at the ship's aerosol inlet changed values of $AOD_{belowJ31}$ by less than 15%, with no systematic bias.

As a check on the above procedure (i.e., Eqs. (1-3)) for calculating $f(RH_{amb}, RH_{neph})$, we also calculated it for representative cases using Eqs. (2-4) of *Wang et al.* [2006], which provide more accurate fits to the RH-scanning measurements of $f(RH, RH_{ref})$ than does our Eq. (1). In these checks we selected from *Wang et al.*'s Eq. (2-4) the one that gave the best fit to the RH-scanning data for the scan time of interest. Comparisons to the results from our Eqs. (1-3) for $f(RH_{amb}, RH_{neph})$ showed absolute differences $<22\%$, with mean differences (*Wang et al.* Eq. (2-4) minus our Eq. (1)) of -2%, -4%, and -7% at 450, 550, and 700 nm. Corresponding rms differences were 5%, 9%, and 11%, respectively.

Because fog was frequently present at the Ron Brown in the 2004 ICARTT measurements, it is important to assess whether fog was present during the periods when we used ship in situ measurements to estimate ambient extinction and AOD below the J31. For three reasons we believe fog was not present during those periods. First, the J31 avoided flying near the Ron Brown when Ron Brown was in fog, for safety reasons. Second, the ship-measured RH_{amb} values during the six periods (78%, 88%, 91%, 83%, 81%, and 84%) were well below 100%. And third,

ship-derived values of liquid water content were zero, and corresponding values of saturation ratio were less than one, during those periods.

2.3 MISR and MODIS

Aerosol measurements from space are essential to understanding aerosol global and regional distributions, temporal variations, transport, and effects on radiation budgets and climate [e.g., *Kaufman et al.*, 2002; *Ramanathan et al.*, 2002]. MISR and MODIS are part of a new generation of spaceborne sensors with capabilities designed specifically to measure aerosols from space, in contrast to their predecessors AVHRR and TOMS (which have provided many useful, though limited, aerosol measurements in spite of not being designed for this purpose). MISR and MODIS were launched on the EOS Terra satellite in 1999, starting a new era of satellite-based observations of aerosols. A second MODIS was launched on the EOS Aqua satellite in 2002. Terra and Aqua are sun-synchronous satellites, with Terra's sunlit overpasses occurring in the local morning and Aqua's in the local afternoon. Equator crossing times for Terra and Aqua are ~10:30 AM and ~1:30 PM, respectively. Advantages of MODIS [*Kaufman et al.*, 1997] over its predecessors AVHRR and TOMS include its improved spectral coverage, narrower bandwidth of individual channels and improved horizontal resolution of 500 m (250 m for some channels), as compared to 1 km or 4 km for AVHRR and 50 km for TOMS. For MISR [*Diner et al.*, 1998, *Martonchik et al.*, 1998], the improved capabilities further stem from its multi-angle viewing technique, which makes it possible to distinguish atmospheric from surface properties and to derive information on particle shape. In particular, the improved spatial resolution of the new sensors allows for a better detection of clouds and hence an improved separation of aerosols from clouds.

Of considerable interest to satellite-based retrievals of AOD is variability on small scales (a few hundred meters or less). The question arises whether an average radiance in a given scene as measured by a satellite sensor can be translated easily into an average AOD over the scene. For example, in preliminary validation studies of the standard MISR AOD retrieval algorithm, *Kahn et al.* [2001b] found that over dark water pixel-to-pixel scene variability could contribute more to

the AOD retrieval uncertainty than MISR camera calibration. In the case of MODIS, spatial variability is of equally great importance. Both the MODIS over-ocean and over-land aerosol retrieval algorithms depend heavily on the spatial variability of radiances and hence also on the variability of aerosol fields in order to detect and mask cloudy pixels [Martins et al., 2002]. In the case of the land algorithm the standard MODIS cloud mask may discard pixels that contain increased AOD in the immediate vicinity of clouds (i.e., less than 500 m away). The ocean algorithm cloud mask uses the spatial variability of the reflectance at 553 nm [Martins et al., 2002]. Hence, suborbital measurements of the actual spatial variability of AOD and tests of the impact of that variability on satellite radiances are crucial in assessing the adequacy of the aerosol retrieval algorithms and the cloud screening procedures used within them. The AOD measurements by AATS on the J31 are well suited to such studies, since they can acquire AOD measurements at a spatial resolution of a few hundred meters and across many satellite retrieval grid cells in a relatively short time (see examples in Section 3)—something not possible in the usual validation studies that use the fixed, ground-based sun/sky photometers in the AERONET network.

In this paper, we describe the AATS-14 measurements of AOD during the 2004 INTEX/ITCT/ICARTT experiment, with a special emphasis on assessing the spatial variability of AOD across multiple satellite retrieval grid cells. We included validation measurements for the MODIS and MISR over-ocean AOD retrieval products. There were four AATS-MISR coincidences, on 20, 22 and 29 July, and on 7 August 2004. In this paper we focus on the 29 July coincidence; the others are described in other papers [e.g., Kahn et al., 2006]. There were eight AATS-MODIS coincidences, on 12, 16, 17, 21, 22 and 23 July, and on 2 and 8 August 2004. We describe all 8 of those coincidences in this paper.

2.3.1 MODIS retrievals of AOD

In the first step of the MODIS over-ocean algorithm for the retrieval of AOD, the reflectances from the six channels at 553, 644, 855, 1243, 1632 and 2119 nm are grouped into nominal 10 km cells of 20 by 20 pixels at 500 m resolution (with the cross-track dimension stretched as distance from the subsatellite track increases). Cloud masking in the over-ocean AOD algorithm is based

on a series of tests that use reflectances at 466, 553, 644, 1243, and 1380 nm. An important test uses the standard deviation of 553 nm reflectances in every group of 3 by 3 pixels within a cell [Remer *et al.*, 2005, Martins *et al.*, 2002]. If any such group has standard deviation greater than 0.0025, the center pixel in the group is initially labeled as cloud. Further tests using other wavelengths are employed to help prevent inhomogeneous aerosol fields (e.g., dust) from being identified as clouds, and to help prevent spatially homogeneous clouds (e.g., cirrus and the centers of large, thick clouds) from being identified as aerosol [e.g., Gao *et al.*, 2002, Remer *et al.*, 2005].

After the application of the various cloud masks, a sediment mask is applied, after which the brightest 25% and darkest 25% (at 855 nm) of the remaining pixels are discarded. The reflectances in the remaining pixels are averaged and compared to a look-up table, consisting of four fine and five coarse mode aerosol types [Remer *et al.*, 2005]. All combinations of fine and coarse modes that fit the measured reflectances to within 3% (or the best three combinations if no solution matches the reflectances to within 3%) are then averaged to yield the average combination of fine and coarse mode aerosol. Over ocean, AOD products are produced at the six measurement wavelengths, 553, 644, 855, 1243, 1632 and 2119 nm, and also at 466 nm by using the model(s) that best fit the measured reflectances.

Initial validation efforts of the MODIS level 2 aerosol data product were carried out by Remer *et al.* [2002, 2005], Levy *et al.* [2003], Livingston *et al.* *et al.* [2003], and Levy *et al.* [2005]. Remer *et al.* [2005] found that one standard deviation of all MODIS-Terra AOD retrievals (when compared to AERONET AOD measurements) fall within the predicted uncertainty $\Delta\tau = \pm 0.03 \pm 0.05 \tau$ over ocean and $\Delta\tau = \pm 0.05 \pm 0.15 \tau$ over land. Recently, Ichoku *et al.*

[2005] validated both MODIS-Terra and MODIS-Aqua aerosol data. They found no significant difference in the performance of MODIS-Terra and MODIS-Aqua for determining AOD between 466 and 855 nm. All these validation studies used the validation approach developed by *Ichoku et al.* [2002], which averages MODIS data over nominally 50 x 50 km boxes and AERONET measurements over 1h. More recently *Redemann et al.* [2006b], working at the nominal Level 2 retrieval scale of 10 km x 10 km, found significant differences between MODIS-Terra and MODIS-Aqua retrievals for both AOD and Ångstrom exponent in terms of their comparison to airborne sunphotometer measurements made in April 2004 in the presence of mineral dust.

The Scientific Data Sets (SDS) within the MODIS level-2 aerosol data products (MOD04_L2 for Terra and MYD04_L2 for Aqua) we specifically consider in this paper are the AOD at 466, 553, 644, 855, 1243, 1632 and 2119 nm [Effective_Optical_Depth_Average_Ocean], the Ångstrom exponent between 553 and 855 nm [Ångstrom_Exponent_1_Ocean(2)], and the Ångstrom exponent between 855 and 2119 nm [Ångstrom_Exponent_2_Ocean(2)]. The index (2) in the Ångstrom exponents denotes that this variable is the average of a number of solutions that best matched the measured radiances, instead of being the single best solution.

2.3.2 MISR retrievals of AOD

MISR produces 36 simultaneous views of Earth, in a combination of nine angles varying from +70° to -70° in the along-track direction, in four spectral bands centered at 0.446, 0.558, 0.672 and 0.867 µm [*Diner et al.*, 1998]. It takes seven minutes for all nine MISR cameras to view a fixed line on the surface, which sets the effective temporal resolution for coincident observations. At midlatitudes, a given location is imaged about once per week in Global Mode, providing 275 m resolution data in all four nadir channels, and in the red channels of the other eight cameras. The remaining 24 channels of data are averaged on board the spacecraft to 1.1 km

resolution. For three MISR event days during ICARTT (20, 22, and 29 July), the Gulf of Maine was also designated as a MISR Local Mode site, 300 km along-track by 360 km cross-track, over which data were acquired at 275 m resolution in all 36 channels.

Pre-launch theoretical studies indicated that MISR spectral radiances, measured at precisely known airmass factors ranging from one to three, could provide tight constraints on AOD over land and water. Due to the wide range of scattering angles sampled (about 50° to 160° at midlatitudes), MISR also offers constraints on particle shape, size distribution, and single scattering albedo, particularly over dark, uniform ocean surfaces [*Kahn et al.*, 2001; *Martonchik et al.*, 1998].

This study is one of many that involve actual field campaign data to assess the sensitivity of aerosol retrievals based on satellite multi-angle imaging. In addition, the assumptions made in the retrieval algorithm about aerosol component particle properties, scene variability, and other factors, must be critically tested and refined. Together with studies from SAFARI, ACE-Asia, and CLAMS [e.g., *Schmid et al.*, 2003; *Kahn et al.*, 2004; *Redemann et al.*, 2005; *Smith et al.*, 2005], the current study is part of an ongoing MISR validation effort that is aimed in part at defining a few satellite scenes very carefully and in detail to then use the findings regarding performance to refine the aerosol retrieval algorithm applied globally. The validation program also compares, statistically, MISR retrieval results with other large aerosol data sets [e.g., *Abdou et al.*, 2005; *Kahn et al.*, 2005]. Since scene variability was determined in pre-launch studies to contribute significantly to the uncertainties in the aerosol retrievals and since AOD variability is one of the main contributors to scene variability over the ocean, the analysis of spatial variability of AOD over multiple MISR retrieval grid cells performed in this paper is expected to support the assessment of MISR aerosol retrieval algorithm performance.

3. Results

3.1 Comparison of AOD above and below the J31 using AATS and ship humidified scattering and absorption

Figure 1 shows results for AOD(500 nm) above and below the J31 for six cases where the J31 flew by the ship at low altitude (60 to 110 m ASL). AOD above the J31 was calculated from AATS measurements as described in Section 2.1. AOD below the J31 was calculated from ship

humidified scattering and absorption measurements as described in Section 2.2, and interpolated to wavelength 500 nm. Note that in all six cases AOD(500 nm) below the J31 is very small compared to AOD(500 nm) above the J31. AOD(500 nm) below the J31 ranged from 0.003 to 0.013, with mean value 0.009 and standard deviation 0.003. These values are comparable to the typical sunphotometer calibration uncertainty of ~ 0.01 (and to the quoted uncertainty of 0.015 for the Ron Brown handheld sunphotometer measurements of AOD; <http://saga.pmel.noaa.gov/data/>). The ratios of AOD(500 nm) below the J31 to AOD(500 nm) above the J31 ranged from 1.0% to 13.9%, with mean value 6.2% and standard deviation 4.8%.

Figure 2 shows AOD spectra above and below the J31 for the six cases in Figure 1. In terms of the ratio of AOD below the J31 to AOD above it, results at 450, 550, and 700 nm are similar to those quoted in connection with Figure 1 for 500 nm. For all six cases Table 1 shows the range, mean, and standard deviation of the ratio of AOD below to above the J31 for all four wavelengths 450, 500, 550, and 700 nm. Including all wavelengths, the mean ratio of AOD below to above the J31 ranged from 5.9% to 6.3% with standard deviation 4.5% to 5.4%.

As noted in Section 2.2, our procedure to obtain the above results for AOD below the J31 neglects any RH_{amb} and aerosol variations with altitude below z_{J31} . On three of the cases shown in Figures 1 and 2 (16 and 29 July and 7 August), radiosonde vertical profiles of RH_{amb} were available near the time of the J31 flyby. For those cases, we used altitude-dependent RH_{amb} in place of the values at the ship's aerosol inlet. Results for $AOD_{belowJ31}$ differed from the values in Figures 1 and 2 by less than 15%, with no systematic bias (i.e., the results with altitude-dependent RH_{amb} were smaller on 16 July and 7 August and larger on 29 July).

Also shown in Figs. 1 and 2 are AOD values measured by handheld sunphotometer on the ship Ron Brown during or close to J31 flybys. Comparisons between the ship sunphotometer AODs and the others are limited by several factors, including lack of perfect coincidence in space and time (see, e.g., the measurement times below the columns in Figure 1). Nevertheless, we feel the comparisons are useful, and that they reveal the following:

- On 3 days (16 and 17 July and 2 August) the difference between AOD(500 nm) from the ship sunphotometers and from AATS (the latter increased by the estimated AOD below the J31) is within the combined measurement uncertainties (0.015 and ~0.01 for the ship sunphotometers and AATS, respectively).
- On the other 3 days (22 and 29 July and 7 August), AATS and ship AOD(500 nm) differ by more than the combined measurement uncertainties. In each of these cases, ship sunphotometer AOD(500 nm) > AATS AOD(500 nm). The sign of the differences (ship AOD > AATS AOD) could be explained by dirt accumulation on the ship sunphotometer windows. However, the ship sunphotometer windows were cleaned prior to each use so this explanation seems unlikely.
- In all these cases (22 and 29 July and 7 August), adding the small estimated AOD(500 nm) below the J31 (0.003 to 0.013) to the AATS values yields too little change to reconcile the AATS-ship AOD differences.
- On 22 July the larger of the MISR AOD retrievals (Version 15) exceeds the AATS AOD and hence agrees better with the ship AOD values. However, on 29 July the opposite is true (i.e., MISR Version 15 AOD < AATS AOD), so MISR AOD disagrees with ship AOD more than with AATS AOD.

In connection with the above comparisons between AATS and ship AOD values it is relevant to mention the considerable history of previous comparisons between airborne AATS AOD measurements and surface-based sunphotometer or radiometer measurements of AOD in several field campaigns [e.g., Schmid et al., 2000 in ACE-2; Schmid et al., 2003 in SAFARI-2000; Livingston et al., 2003 in PRIDE, Redemann et al., 2005 in CLAMS and Schmid et al., 2006 in DOE-ARM AIOP), which showed very good agreement (i.e., RMS differences ≤ 0.01). In the current study we have not used ship-estimated AOD below the J31 to increase AATS-measured AODs, because the ship-estimated AODs are small (mean 0.009 at 500 nm), varied significantly (from 0.003 to 0.013 at 500 nm), covered only a small subset of AATS wavelengths (450-700 nm out of 354-2119 nm), and were not available for many AATS low-altitude transects.

3.2 MISR-AATS comparisons

Figure 3 shows a MISR image from the overpass on 29 July 2004 at 1534 UT (15.57 UT in decimal hours), along with the J31 flight track. (In this paper, all times with decimal points are in decimal hours, and times without decimal points are HHMM, where HH is hours and MM is minutes. We use both because decimal hours provide the most convenient time axis in plots, whereas satellite and other data are often archived in HHMM format. All times in this paper are in Universal Time (UT).) The MISR image, from camera Aa (i.e., looking forward along the satellite track at 26° from nadir) shows the Gulf of Maine off the New Hampshire and Maine coasts, as well as the clouds that were prevalent on this day (and on many other days during ICARTT). The J31 track (right frame of Figure 3) includes a minimum-altitude path in the shape of a right triangle (i.e., with contiguous legs at right angles to each other), flown during the period ~ 15.38 – 17.00 UT. The original flight plan had the right angle at a different location, but the plan was adjusted after takeoff to move the minimum-altitude legs to areas that were as cloud-free as possible.

Figure 4 (top frame) shows a more detailed view of the minimum-altitude J31 legs. In this view, any point along the J31 path is omitted if clouds are impacting AATS's view of the sun, and also if the J31 altitude exceeds 100 m (which typically occurred during J31 turns). It can be seen that the AATS viewing path was cloud-impacted at Terra overpass time (15.57 UT), but largely cloud-free on the legs before and after that time. All AATS measurements considered in this section were taken within ± 30 minutes of satellite overpass time.

Also shown in Figure 4 (top frame) are the grid cells in which MISR Standard Algorithm AOD retrievals were possible. The J31 flew through 8 such MISR grid cells at altitudes ≤ 100 m and within ± 30 minutes of satellite overpass time. Figure 4 (bottom frame) shows AATS-measured multiwavelength AODs along the J31 track flown from ~ 15.25 to 16.0 UT. These results show a strong gradient in AOD, with AOD(499 nm) decreasing from ~ 0.8 to ~ 0.38 when flying west along the northernmost leg (15.6 to ~ 15.77 UT), and then increasing from ~ 0.38 to ~ 1.1 when

flying east-southeast along the southern leg (15.79-16.0 UT). Colored vertical lines in Figure 4 (bottom frame) show the times when the J31 crossed the edge of a MISR grid cell. The colors of the vertical lines in Figure 4 (bottom frame) match those of the grid cells in the top frame. (Absence of a grid cell along a J31 flight segment indicates absence of a MISR Standard Aerosol retrieval there. Currently, the Standard algorithm requires that at least 32 of 256 1.1 km pixels in each 17.6 x 17.6 km cell must pass tests for cloud masking, spatial correlation, and angular smoothness.)

Figure 5 compares AATS and MISR V15 AOD spectra. A MISR spectrum is shown for each of the 8 colored grid cells in Figure 4. AATS spectra are shown in this figure only as the mean from the whole flight path of Figure 4, along with the typical AATS measurement uncertainty (narrow ticks), standard deviation of results along the flight path (wide ticks), and range along the flight path (vertical bars). The inset time series in Figure 5 shows that MISR V15 spectra have the same sign of gradient as AATS. For example, the inset time series shows AATS AOD decreasing in going from red cell to yellow cell to green cell to blue cell. The MISR spectra in the main figure show the same thing: decreasing AOD in going from red spectrum to yellow spectrum to green spectrum to blue spectrum.

Figure 6 shows the analogous comparison for MISR V16. V16 retrieved AOD in only 7 cells; however, they show a gradient with the same sign as AATS AOD, analogous to that described above. The V16 MISR Standard Aerosol Retrieval algorithm contains improved medium-mode dust optical models [Kalashnikova *et al.*, 2005], and additional medium-mode spherical particles having single-scattering albedo 0.80 and 0.90, that replace the tiny black carbon particles in earlier algorithm versions.

Figure 7 uses scatter plots (one for each MISR wavelength) to make a more quantitative comparison of MISR V15 and AATS AODs and their gradients. AATS AODs for each grid cell were obtained by averaging all AATS measurements within the cell to yield a spectrum of \ln AOD vs. $\ln \lambda$, which was then fitted with a quadratic least-square fit. From the AATS-derived fit, the AOD at the intermediate MISR wavelengths of 446, 558, 672 and 867 nm was determined. Although several MISR wavelengths are close to AATS-14 wavelengths (cf. Figs. 5

and 6), the fit procedure above was used to minimize the impact of possible AATS-14 single-channel contamination and other uncertainties. and uncertainties stemming from gaseous absorption in the AATS channels, the latter being particularly important at the near-IR wavelengths.

The positive slopes and large R^2 values in Figure 7, 0.91 to 0.92, confirm that MISR V15 is obtaining the same sign of AOD gradient as AATS. However, the fact that the slopes are <1 (0.77 to 0.80) shows that the MISR gradient is somewhat weaker than the AATS gradient. The relatively large AOD values (AATS AOD(446 nm)~0.4 to 1.0) and different gradients produce RMS MISR-AATS differences of 0.03 to 0.07 (9 to 11%).

Figure 8 shows analogous scatter plots for MISR V16. In this case slopes range from 0.72 to 0.88, and RMS MISR-AATS differences are 0.03 to 0.21 (11 to 31%).

Taken together, Figs. 5-8 show that, for the 29 July 2004 MISR-AATS comparison, MISR V15 is closer to AATS than is V16, in terms of both Ångstrom exponent (slope in Figs. 5 and 6) and in AOD for most wavelengths (RMS differences in Figs. 7 and 8). The larger Ångstrom exponent of MISR V15 AOD results from the V15 retrieved aerosol mixture having smaller particles than V16. The V15 Standard Retrieval mixtures are primarily non-absorbing spheres with r_{eff} 0.26 μm , with small fractions of spheres with r_{eff} ~0.12 and 0.57 μm , and black carbon in some cases. The V16 Standard Retrieval mixture is about half non-absorbing, r_{eff} 0.26 μm spheres and half medium dust.

Caveats to bear in mind regarding the 29 July MISR-AATS comparison include the fact that variability dominates this comparison and that there was no MISR retrieval in exact AATS-coincident pixels due to cloud contamination. It is also noteworthy that V15 and V16 AOD values were fairly similar in pixels near the J31 path, but V16 Ångstrom exponent increases in nearby MISR cells.

A conjecture is that V16 picks up as “dust” an r_{eff} >0.26 μm or non-spherical component. This could be cirrus or a medium spherical particle mixture not in the V16 climatology. A newer

version, V19, may yield improvement over V16 by including aerosol mixtures having 100% medium-mode spherical particle mixtures available in V15 but not in V16. These issues are explored further using the MISR Research Aerosol Retrieval algorithm in a companion paper [Kahn et al., 2006].

3.3 MODIS-AATS AOD comparisons

AATS underflew MODIS-Terra and MODIS-Aqua several times in ICARTT. For 3 Terra and 5 Aqua overpasses, MODIS standard aerosol retrievals were made in 61 MODIS grid cells that contained low-altitude, cloud-free AATS flight segments (for Terra: 17 cells on 17 and 22 July and 2 August; for Aqua: 44 cells on 12, 16, 21, and 23 July and 8 August). We first illustrate the MODIS-AATS comparisons by presenting in detail one day, 21 July 2004, and then summarize all the MODIS-AATS comparisons in terms of scatter plots.

All AATS measurements considered in this section were taken within ± 30 minutes of satellite overpass time and at J31 altitudes below 100 m, with the following exceptions. For the 12 July Aqua overpass we have included 4 cells with J31 altitude between 100 and 190 m, because the MODIS-AATS comparisons in those cells were virtually identical to that in the single cell with J31 altitude <100 m. For the 16 July Aqua overpass we have included 3 cells with J31 altitude between 100 and 250 m, because the MODIS-AATS comparisons in those cells were virtually identical to that in the single cell with J31 altitude <100 m. For the 2 August Terra overpass we have included 2 cells with J31 measurement time extending to 31 and 33 minutes after Terra overpass time, because the AATS AOD spectra in those cells were virtually identical to those in the 7 cells with J31 measurements within 30 minutes of Terra overpass.

Figure 9 (left frame) shows the 21 July 2004, 18.10 UT MODIS-Aqua true color image of the New England coastal area in the vicinity of the J31 base (Pease International Tradeport, New Hampshire, near the coast on the Gulf of Maine). Note the grayish haze at the bottom left-middle of the frame, extending Northeastward over Cape Cod and toward the Gulf of Maine. The larger-area MODIS image (not shown) reveals that this grayish haze is part of a large smoke plume stretching from Canada into the central US, then curving E over the coastal Atlantic, N off the

mid-Atlantic states and Long Island, and NE into the New England coastal area. The MODIS web site identified the plume as smoke from the Alaska wildfires of 2004, a description consistent with many aircraft measurements in ICARTT [e.g., *Fehsenfeld et al.*, 2006]. Also shown in the MODIS image are the white scattered clouds over land and the larger clouds over the Gulf of Maine, some of which appear grayish (see further discussion below).

Figure 9 (right frame) shows the J31 flight track for 21 July. Arrows between left and right frames connect coastal features. Figure 10 shows a more detailed view of the J31 track, with 13 grid cells of MODIS aerosol retrievals superimposed. The inset shows J31 altitudes vs. time.

Figure 11 shows vertical profiles of multiwavelength AOD and extinction from AATS measurements on the initial ascent out of Pease and on spiral descent 1. (See locations of the ascent and descent marked in Figure 10.) As noted in Section 2.1, each AATS extinction profile is obtained by vertically differentiating a spline fit to the corresponding AOD profile. Note in the left extinction profile a layer at ~5 km altitude, which is missing in the right extinction profile. Because analyses from other aircraft in the area [e.g., *Fehsenfeld et al.*, 2006] showed the Alaska-Canada smoke to be layered at altitudes ~5 km, we identify the extinction layer at ~5 km as being from this smoke, which was evidently present at the location of initial ascent, but not at spiral descent 1 (cf. Figs. 9-10).

Figure 12 shows a detailed view of the low-altitude J31 flight path and the 13 MODIS grid cells along it, together with time series of J31 altitude and AATS-measured AOD and column water vapor (CWV). Colored vertical lines on the AOD vs. time plot show edges of MODIS grid cells, and colored horizontal arrows span the time segment the J31 spent in each grid cell. Note the increase in AOD during 18.30-18.37 UT, when the J31 flew from the pink MODIS cell, into and across the green cell, and into the blue cell. This AOD increase occurs as the J31 flies toward the location of the ascent out Pease (which had the extinction layer at ~5 km altitude, Figure 11) and away from the location of spiral descent 1 (which was missing this layer). Thus, the most likely reason for the AOD increase is that the J31 is flying into the region covered by the elevated smoke plume. *Redemann et al.* [2006b] explore the impacts of this and other AOD gradients on radiative fluxes, deriving radiative forcing efficiencies.

Figure 13 compares AOD spectra from the 13 MODIS grid cells in Figs. 10 and 12 with the AOD spectrum from AATS averaged along the flight path. Also shown are the AATS AOD uncertainty (narrow ticks), standard deviation along the flight path (wide ticks), and range (vertical bars with no ticks). AATS AOD spectra from the 13 individual MODIS cells are shown in Figure 14, each compared to the corresponding MODIS AOD spectrum.

Note that the MODIS retrievals in Figure 13 show an AOD gradient with the sign of the AATS AOD gradient (i.e., MODIS AOD increases in going from pink cell to green to blue), but that the blue-cell MODIS AODs exceed the AATS AODs by more than the combined uncertainties at wavelengths 553-1243 nm. Our analyses indicate that the large MODIS AODs in the blue cell are caused by cloud contamination, which is enabled by smoke over cloud impairing the MODIS cloud mask. Following is the evidence on which we base this conjecture. First note the gaps in the AATS AOD traces, 18.36-18.38 UT in Figure 12 (also indicated by gaps in the J31 flight track in the blue cell). These gaps are caused by clouds intermittently blocking the AATS-to-sun viewing path. As noted in Section 2.1, the AATS processing algorithm detects these clouds via their effect on the time variation of AATS detector signals (specifically the standard deviation of detector output voltages measured at 3 Hz over a 3-second period). It then excludes such signals from AOD analysis. As noted in Section 2.3.1, the MODIS cloud screen uses the standard deviation of 553 nm reflectances in groups of 3 by 3 pixels [Remer *et al.*, 2005; Martins *et al.*, 2002]. However, if smoke over cloud reduces this standard deviation (by reducing reflectances over cloud and increasing them over cloud-free pixels), some cloudy pixel groups could have their standard deviation drop below the cloud threshold of 0.0025, and hence escape detection. Inclusion of such pixel groups in the AOD retrieval would artificially increase AOD values.

Additional evidence for this process is given by the MODIS grid cell cloud fractions and Ångstrom exponent values. Of the 13 cells in Figs. 10, 12, and 14, all but 3 report ‘no clouds’ and use all the available pixels to make the retrieval. The three exceptions are the blue cell (centered at 43.088 °N), which reports 53% clouds, and two cells at the opposite end of the group, i.e., the red cell (centered at 43.423° N), which reports 8% clouds, and the black cell (centered at 43.531 °N), which reports 14% clouds. In other words, in a nearly cloud-free set of

13 cells, the blue cell reports the largest cloud fraction, 53%. Smoke over the clouds in such a cell could very well smooth out the reflectance variability of the clouds. Another possibility is clouds scattering light out of the sides of clouds, a situation previously analyzed by *Wen et al.* [2006].

Regarding MODIS Ångstrom exponent values, notice in Figure 14 that they decrease in going from the pink and green cells to the blue cell. This is true for both wavelength ranges, 553-855 nm and 855-2119 nm, but especially so for the longer wavelength range, which would be most affected by reflectance from cloud particles. Specifically, for 553-855 nm, the MODIS Ångstrom exponent in the blue cell, 1.43, is 4% less than the average value in the pink and green cells, 1.49; for 855-1219 nm, the corresponding decrease is 12%, from 2.12 to 1.86. In contrast, the AATS Ångstrom exponent for 553-855 nm in the blue cell, 1.62, is only 0.5% less than the red-green average, and the corresponding change for 855-1219 nm is actually a 7% increase, from 1.73 to 1.86—possibly caused by the elevated smoke plume having smaller particles than the haze below. Because the cell-to-cell differences in MODIS Ångstrom exponent described here are relatively small (i.e., <0.26), they may not be significant enough to constitute proof of cloud contamination, but they are consistent with cloud contamination and do provide supporting evidence. See also Section 3.4.

We have also checked the data-quality flags for each of the 13 cells in Figs. 10, 12, and 14. Twelve of the 13 cells have QA=3 (indicating high data quality), including the 3 squares mentioned above with some cloud fraction. There is one square with QA=1 (low quality) because it had some difficulty fitting a model. This is the cell centered at 43.478° N, but its AOD spectrum is very similar to its neighbors, and there is no reason to eliminate it.

Figure 15 presents scatter plots comparing MODIS and AATS AODs for the 21 July case. Also shown are the MODIS uncertainty estimates of $\Delta\tau = \pm 0.03 \pm 0.05\tau$ as blue lines. As with the MISR-AATS comparisons, AATS AODs for each grid cell were obtained by averaging all AATS measurements within the cell to yield a spectrum of $\ln \text{AOD}$ vs. $\ln \lambda$, which was then fitted with a quadratic least-square fit (exemplified by the thin black curves in Figure 14). From the AATS-derived fit, the AOD at the intermediate MODIS wavelengths of 466, 553, 644, 855,

1243, 1632 and 2119 nm was determined. Although several MODIS wavelengths are close to AATS-14 wavelengths (cf. Figure 14), the fit procedure above was used to minimize the impact of possible AATS-14 single-channel contamination, calibration uncertainties and uncertainties stemming from gaseous absorption in the AATS channels, the latter being particularly important at the near-IR wavelengths.

The plot on the left in Figure 15 includes all 13 MODIS grid cells, whereas the plot on the right excludes the blue cell that is suspected of cloud contamination. Comparing the two shows how excluding the blue cell reduces the RMS difference between MODIS and AATS results (from 0.033 to 0.029, or from 20.4% to 18.6%), and increases R^2 (though negligibly, from 0.992 to 0.993). The percentage of MODIS AOD retrievals within $\Delta\tau = \pm 0.03 \pm 0.05\tau$ of the AATS values increases from 80% to 83% when the blue cell is excluded; the fraction of near-IR retrievals (855-2119 nm) increases from 96 to 98%.

As mentioned above, in ICARTT there were 61 MODIS standard aerosol retrieval grid cells that (1) produced MODIS AOD spectra and (2) contained J31 low-altitude flight segments that provided AATS AOD values (17 cells from 3 Terra overpasses, and 44 cells from 5 Aqua overpasses). Figure 16 presents scatter plots comparing MODIS and AATS AODs for these 61 cases (including the 21 July MODIS-Aqua cell suspected of cloud contamination), separated into Aqua and Terra cases. About 87% of the MODIS AOD retrievals differ from AATS AODs by less than the predicted MODIS over-ocean uncertainty, $\Delta\tau = \pm 0.03 \pm 0.05\tau$; the fraction of near-IR retrievals that fall within this uncertainty range is about 93%. When all MODIS wavelengths are included, RMS MODIS-AATS AOD differences are 0.028 (20%) for MODIS-Aqua and 0.030 (21%) for MODIS-Terra. When wavelengths are restricted to 466, 553, 644, and 855 nm, the RMS AOD differences become 0.036 (25%) for MODIS-Aqua and 0.036 (25%) for MODIS-Terra. R^2 values for all 4 cases are between 0.964 and 0.972.

3.4 MODIS-AATS Ångstrom exponent comparisons

Similar to the methodology used for the AOD comparisons in the previous section, we determined Ångstrom exponents from the AATS-14 measurements within each MODIS retrieval

cell by first averaging all cloud-free, low-altitude AATS-14 AOD measurements in the cell, then fitting the spectrum of $\ln\text{AOD}$ vs. $\ln\lambda$ with a quadratic, and finally calculating the Ångstrom exponents from the ratios of the fitted AOD values, τ_{fit} , at the respective wavelengths, i.e.,

$$\alpha = -\frac{\ln[\tau_{fit}(\lambda_1)/\tau_{fit}(\lambda_2)]}{\ln(\lambda_1/\lambda_2)} \quad (7)$$

where the wavelength pairs are 553 and 855 nm for the first and 855 and 2119 nm for the second Ångstrom exponent, respectively.

Figure 17 (left frame) shows a scatter plot comparison of Ångstrom exponents for 553-855 nm and 855-2119 nm for MODIS-Terra and MODIS-Aqua. In general there is very poor agreement between the Ångstrom exponents from AATS-14 and MODIS. In most cells the MODIS-derived Ångstrom exponents exceed the AATS-derived values, for both 553-855 nm and 855-2119 nm. This is especially so when AATS $\alpha(855-2119) < \sim 1$ or when AATS $\alpha(553-855) < \sim 1.6$. The RMS differences between AATS-14 and MODIS-derived 553-855 nm Ångstrom exponents are 0.28 (21%) for MODIS-Terra and 0.66 (43%) for MODIS-Aqua; the RMS differences between AATS-14 and MODIS-derived 855-2119 nm Ångstrom exponents are 0.61 (45%) for MODIS-Terra and 1.18 (92%) for MODIS-Aqua. None of the four correlation coefficients has $R^2 > 0.7$.

Many of the above results for MODIS-AATS Ångstrom comparisons are quite similar to those reported by *Redemann et al.* [2006b] for measurements off the US West coast in April 2004. At first the large differences between AATS and MODIS Ångstrom exponents may seem surprising given the very small differences between AATS and MODIS AOD values (cf. Figure

16, RMS differences ~ 0.04 (19% to 26%). However, one must bear in mind that the uncertainty in an Ångstrom exponent depends directly on the relative uncertainties in the associated AOD values, which increase as AOD decreases. Although most of the AOD points in Figure 16 fall within the MODIS over-ocean uncertainty estimates of $\Delta\tau = \pm 0.03 \pm 0.05\tau$, many AOD values are < 0.1 , with MODIS AOD uncertainties of 30% to 100% or more. These large AOD relative uncertainties propagate to large Ångstrom absolute uncertainties, as has been previously noted by *McArthur et al.* [2002]. This is illustrated by Figure 18, which shows MODIS-AATS Ångstrom exponent differences as a function of AATS AOD. Note that the largest differences are associated with the smallest AOD values.

This is further illustrated by Figure 19, which shows AATS and MODIS AOD spectra for the 15 MODIS-Aqua grid cells for the 17.90 UT Aqua overpass on 8 August 2004, a case with AOD < 0.1 for all $\lambda > 400$ nm. These spectra and their associated Ångstrom exponent values illustrate how AOD values can agree within error bars for all wavelengths and still produce Ångstrom exponents that differ by 1 to 2 or more if the relative error bars for AOD are large enough.

To illustrate the effect of excluding cases with small AOD, the right frame of Figure 17 shows the MODIS-AATS Ångstrom scatter plot for all cells except those with AATS AOD(855) < 0.1 . This exclusion markedly reduces RMS differences between MODIS and AATS Ångstrom exponents; however, the reduced range of AATS Ångstrom exponent values reduces most R^2 values as well.

Anderson et al. (2005) also compared Ångstrom exponents from MODIS and airborne sunphotometer, using data from April 2001 near Japan and Korea involving varying mixtures of dust, sea salt, and pollution. As in the current study and *Redemann et al.* [2006b], *Anderson et al.*

[2005] found that Ångstrom exponents from MODIS were systematically larger than those from airborne sunphotometer. However, RMS differences found by *Anderson et al.* were only 0.14, considerably less than the RMS differences found in the current study (0.3 to 1.2) or by *Redemann et al.* [0.2 to 0.7]. The fact that the Anderson et al. midvisible AODs (0.25 to 0.45 at 550 nm) included none of the small AODs of the *Redemann et al.* and current studies may help explain the relatively small RMS differences found by *Anderson et al.* (The midvisible AOD range for *Redemann et al.* was 0.13 to 0.3; for the MODIS-AATS comparisons of the current study it was 0.06 to 0.66.) However, relatively large AODs do not ensure small differences between MODIS and suborbital results for Ångstrom exponent; other studies [e.g., *Levy et al.*, 2003; *Livingston et al.*, 2003] have found MODIS retrievals of Ångstrom exponent that differed significantly from suborbital results, possibly as a result of dust nonsphericity.

As a final note on MODIS Ångstrom exponent comparisons, we report that we have repeated all the above analyses, using MODIS Ångstrom exponents from the single best solution in place of the average of a number of solutions that best matched the measured radiances, i.e., substituting MODIS [Ångstrom_Exponent_1_Ocean(1)] for [Ångstrom_Exponent_1_Ocean(2)], and [Ångstrom_Exponent_2_Ocean(1)] for [Ångstrom_Exponent_2_Ocean(2)]. The results (not shown for brevity) show that:

- Using the single-best-solution set of MODIS Ångstrom exponents produces scatter plots very similar to those in Figure 17, but with most RMS MODIS-AATS differences slightly smaller than those for the average of best solutions.
- When AOD is small (e.g., on 8 Aug, Figure 19), large cell-to-cell jumps in $\alpha(855-2113 \text{ nm})$ occur for both the single-best-solution and average-of-best-solutions sets of MODIS Ångstrom exponent.

From this we conclude that the single-best-solution set of MODIS Ångstrom exponents is slightly more accurate than the average-of-best-solutions set, and that use of the average-of-best-solutions set does not protect against large cell-to-cell jumps in $\alpha(855-2113 \text{ nm})$ when AOD becomes small enough.

3.5. Experiments with extending MODIS retrievals into the glint mask

Sunglint is the specular reflection of sunlight from the sea surface. All MODIS AOD results shown so far in this paper were obtained using the standard MODIS glint mask, which excludes from the AOD retrieval all pixels for which the glint angle ψ is $<40^\circ$. For each pixel, ψ is defined as the angle between two light paths: the pixel-to-satellite path and the path of specular reflection of the solar beam assuming the pixel is a horizontal mirror.

On 29 July 2004 the J31 underflew both Terra and Aqua, and its flight path was within the standard MODIS glint mask (i.e., ψ was $<40^\circ$) for both MODIS-Terra and MODIS-Aqua. Hence, the MODIS standard algorithm with the standard glint mask produced no AOD retrievals along the J31 flight path. To test whether MODIS AOD retrievals could succeed within the standard mask, we ran the AOD algorithm with the glint mask reduced below its normal cutoff of 40° . Figure 20 shows an example of the resulting AOD retrievals, in this case with both the MODIS-Terra and MODIS-Aqua glint masks reduced to 25° . Figure 21 shows the J31 flight path, with low-altitude segments flown near the Terra and Aqua overpass times (1534 and 1715 UT) indicated. (At 1534 UT the J31 was on the low-altitude path shown; at 1715 it was in a spiral, after which it flew the indicated low-altitude leg from 1727 to 1737 UT.)

Figs. 22 and 23 show the MODIS retrieval grid cells along the J31 low-level legs and compare the resulting MODIS AOD retrievals to the AATS AOD results. Glint angles within the MODIS-Terra cells shown range from 29.3° to 34.7° . For the MODIS-Aqua cells shown they range from 32.0° to 33.0° . Note that the MODIS AOD spectra systematically underestimate the AATS spectra, especially at the longer wavelengths. The sign of these AOD differences (MODIS AOD < AATS AOD) is consistent with wind speeds measured on board the NOAA R/V Ronald Brown (located as shown in Figure 21). Specifically, wind speed on the R/V Brown was 0.7 m s^{-1} at Terra overpass time and 3.4 m s^{-1} at Aqua overpass time. These speeds are both less than the 6 m s^{-1} assumed by the MODIS AOD retrieval algorithm in computing surface reflectance within the glint mask (using a rough-ocean model, as described by *Tanre et al.* [1999]). Hence, the MODIS AOD retrievals assume more ocean reflectance than is actually present in these cases, and must retrieve less-than-actual AOD to match the observed radiances. Comparing Figs. 22 and 23 shows that the MODIS-AATS AOD differences are less for MODIS-Aqua than for MODIS-Terra. This is consistent with the ship-measured increase in wind speed, from 0.7 m s^{-1} at Terra overpass time to 3.4 m s^{-1} at Aqua overpass time. In other words, wind speed at Aqua overpass time is closer to the assumed 6 m s^{-1} , leading to less underestimation in retrieved AOD.

The fact that significant underestimation in MODIS-retrieved AOD is obtained even for the cell with the largest glint angle, 34.7° , in Figure 22, indicates that the standard MODIS glint mask cutoff angle, 40° , should not be reduced by as much as 5° below its current value. This is consistent with Figure 15 of *Tanre et al.* [1999], which shows glint-induced errors in AOD (from the MODIS airborne simulator) increasing rapidly for glint angle decreasing from 38° to 34° .

4. Summary and conclusions

Sunphotometer measurements on low-altitude J31 transects in Summer 2004 provided AOD spectra for comparison to satellite retrievals in 29 MISR grid cells (on 20, 22, 29 July and 7 August), in 17 MODIS-Terra standard AOD retrieval grid cells (on 17, 22 July and 2 August), and 44 MODIS-Aqua standard AOD retrieval grid cells (on 12, 16, 21, 23 July and 8 August), plus 14 MODIS-Terra and 6 MODIS-Aqua cells that were excluded by the standard MODIS glint mask on 29 July. Each grid cell had J31 altitude 60 to 100 m and AATS measurements within ± 30 minutes of satellite overpass time, with several exceptions: 7 grid cells where J31 altitude was as high as 110 to 250 m and 2 cells with J31 measurement time extending to 31 and 33 minutes after satellite overpass. In each exceptional cell the AATS-satellite AOD comparisons were essentially the same as in neighboring cells where J31 altitude was < 100 m and AATS measurement time was within ± 30 minutes of satellite overpass.

Ship measurements of humidified light scattering and absorption during six J31 flybys were used to estimate AOD below the J31. In all six cases the estimated midvisible AOD below the J31 was < 0.014 (typically < 0.01) when the J31 was at the typical altitude of 60 to 100 m ASL used in its low-altitude transects. These values are comparable to the typical sunphotometer calibration uncertainty of ~ 0.01 (and to the quoted uncertainty of 0.015 for the Ron Brown handheld sunphotometer measurements of AOD; <http://saga.pmel.noaa.gov/data/>). The ratios of AOD(500 nm) below the J31 to AOD(500 nm) above the J31 ranged from 1.0% to 13.7%, with mean value 6.2% and standard deviation 4.8%. Including four wavelengths, 450-700 nm, the mean ratio of AOD below to above the J31 ranged from 5.9% to 6.3% with standard deviation 4.5% to 5.4%.

This paper presents results for MISR-AATS AOD comparisons on 29 July 2004 in 8 grid cells (each 17.6 km x 17.6 km). On this day AATS measurements in the MISR footprint showed a strong AOD gradient, with AOD(500 nm) changing by as much as 0.13 per 10 km in the horizontal. MISR-AATS AOD comparisons show that MISR Version 15 and 16 retrievals also documented a gradient: MISR and AATS AODs were highly correlated, with $R^2 = 0.87$ to 0.92. However, the MISR gradient was somewhat weaker than the AATS gradient. The large AOD (midvisible values up to ~ 0.8) and differing gradients in this case produced root-mean-square (RMS) MISR-AATS AOD differences of 0.03 to 0.21 (9 to 31%). MISR V15 Ångström exponent α was closer to AATS than was MISR V16. MISR-AATS comparisons on the other 3

days are presented in other papers [e.g., *Kahn et al.*, 2006]. Taken together, these analyses are being used to improve the MISR retrievals, including their information on such aerosol microphysical properties as size and absorption.

MODIS-AATS AOD comparisons on 8 overpasses using the standard MODIS glint mask in 61 grid cells (each nominally 10 km x 10 km) had $R^2 \sim 0.97$, with RMS AOD difference ~ 0.03 ($\sim 20\%$). About 87% of the MODIS AOD retrievals (89% for Aqua, 81% for Terra) differed from AATS values by less than the predicted MODIS over-ocean uncertainty, $\Delta\tau = \pm 0.03 \pm 0.05\tau$. In contrast to the small MODIS-AATS differences in AOD, MODIS-AATS differences in Ångstrom exponent α were large: RMS differences for $\alpha(553, 855 \text{ nm})$ were 0.28 for MODIS-Terra and 0.64 for MODIS-Aqua; RMS differences for $\alpha(855, 2119 \text{ nm})$ were larger still: 0.61 for MODIS-Terra and 1.14 for MODIS-Aqua. None of the four correlation coefficients for Ångstrom exponent had $R^2 > 0.7$. The largest MODIS-AATS Ångstrom exponent differences were associated with small AOD values, for which MODIS AOD relative uncertainty is large. Excluding cases with $\text{AOD}(855 \text{ nm}) < 0.1$ reduced MODIS-AATS α differences markedly; resulting RMS differences for $\alpha(553, 855 \text{ nm})$ were 0.18 for MODIS-Terra and 0.13 for MODIS-Aqua; RMS differences for $\alpha(855, 2119 \text{ nm})$ were 0.46 for MODIS-Terra and 0.41 for MODIS-Aqua.

In one grid cell on 21 July 2004, smoke over cloud appeared to impair the MODIS-Aqua cloud mask, resulting in retrieved AODs that significantly exceeded the AATS values. Evidence for cloud effects on MODIS AOD in this case includes not only AOD values but also differences in Ångstrom exponents and an increased cloud frequency in both the AATS data record and in the MODIS retrieval itself.

Experiments with extending MODIS retrievals into 14 MODIS-Terra and 6 MODIS-Aqua cells within the standard MODIS glint mask on 29 July yielded MODIS AODs consistently less than AATS AODs, especially at long wavelength, indicating that the current MODIS glint mask limits should not be reduced to the extent tried here. The sign of these AOD differences (MODIS AOD < AATS AOD) is consistent with wind speeds measured on board the NOAA R/V Ronald Brown. The fact that the MODIS-AATS AOD differences within the glint mask were less for

MODIS-Aqua than for MODIS-Terra is consistent with the ship-measured increase in wind speed, from 0.7 m s^{-1} at Terra overpass time to 3.4 m s^{-1} at Aqua overpass time.

Acknowledgements

This research is a contribution to the International Consortium for Atmospheric Research on Transport and Transformation (ICARTT), which includes Phase A of the Intercontinental Chemical Transport Experiment (INTEX-A) of the National Aeronautics and Space Administration (NASA) and the Intercontinental Transport and Chemical Transformation (ITCT) experiment of the National Oceanic and Atmospheric Administration (NOAA). The AATS-14 measurements were supported by NOAA's Atmospheric Composition and Climate Program and by NASA's Programs in Radiation Science, Suborbital Science, and Tropospheric Chemistry. The analyses were supported by NASA's Earth Observing System Inter-Disciplinary Science (EOS-IDS) Program. The work of R. Kahn is supported in part by NASA's Climate and Radiation Research and Analysis Program, under H. Maring, and in part by the EOS-MISR instrument project; it is performed at the Jet Propulsion Laboratory, California Institute of Technology, under contract with NASA.

References

- Abdou, W.A., D.J. Diner, J.V. Martonchik, C.J. Bruegge, R.A. Kahn, B.J. Gaitley, K.A. Crean, L.A. Remer, and B. Holben, 2005, Comparison of coincident MISR and MODIS aerosol optical depths over land and ocean scenes containing AERONET sites, *J. Geophys. Res.*, doi:10.1029/2004JD004693.
- Anderson, T. L., and J. A. Ogren, Determining aerosol radiative properties using the TSI 3563 integrating nephelometer, *Aerosol Sci. Technol.*, 29, 57–69, 1998.
- Anderson T. L., Y. Wu, D. A. Chu, B. Schmid, J. Redemann, O. Dubovik. Testing the MODIS satellite retrieval of aerosol fine-mode fraction. *J. Geophys. Res.*, 110, D18204, doi:10.1029/2005JD005978, 2005.
- Bucholtz, A., Rayleigh-scattering calculations for the terrestrial atmosphere, *Appl. Opt.*, 34, 2765-2773, 1995.

- Carrico, C., P. Kus, M. Rood, P. Quinn, and T. Bates, Mixtures of pollution, dust, seasalt, and volcanic aerosol during ACE-Asia: Aerosol radiative properties as a function of relative humidity, *J. Geophys. Res.*, *108*, D23, 8650, doi: 10.1029/2003JD003405, 2003.
- Chu, D. A., Y. J. Kaufman, C. Ichoku, L. A. Remer, D. Tanre and B. N. Holben, Validation of MODIS aerosol optical depth retrieval over land. *Geophys. Res. Lett.*, **29**, art. no.- 1617, 2002.
- Chu, D. A., L. A. Remer, Y. J. Kaufman, B. Schmid, J. Redemann, K. Knobelspiesse, J.-D. Chern, J. Livingston, P. B. Russell, X. Xiong, and W. Ridgway. Evaluation of aerosol properties over ocean from Moderate Resolution Imaging Spectroradiometer (MODIS) during ACE-Asia. *J. Geophys. Res.*, *110*, D07308, doi:10.1029/2004JD005208, 2005.
- Clough, S. A., and M. J. Iacono, Line-by-line calculations of atmospheric fluxes and cooling rates II: Application to carbon dioxide, ozone, methane, nitrous oxide, and the halocarbons, *J. Geophys. Res.*, *100*, 16,519-16,535, 1995.
- Diner, D.J., et al., Multiangle Imaging Spectroradiometer (MISR) description and experiment overview, *IEEE Trans. Geosci. Remote Sens.*, *36*, 1072-1087, 1998.
- Edwards, A. L., "The Correlation Coefficient." Ch. 4 in *An Introduction to Linear Regression and Correlation*. San Francisco, CA: W. H. Freeman, pp. 33-46, 1976.
- Fehsenfeld, F. C., et al., International Consortium for Atmospheric Research on Transport and Transformation (ICARTT): North America to Europe: Overview of the 2004 summer field study, *J. Geophys. Res.*, ICARTT special section, submitted 2006.
- Gao, B.-C., Kaufman, Y. J., Tanré, D. and Li, R.-R.: Distinguishing tropospheric aerosols from thin cirrus clouds for improved aerosol retrievals using the ratio of 1.38- μm and 1.24- μm channels., *Geophys. Res. Lett.*, *29*, 1890, doi:10.1029/2002GL015475, 2002.
- Gassó, S., O'Neill, N. T., and Redemann, J., Passive remote sensing of aerosol fine mode fraction: A comparison with in-situ measurements during the ACE-Asia field campaign, *Eos Trans. AGU*, *85*(47), Fall Meet. Suppl., Abstract A33D-0095, 2004.
- Gassó, S., and N. O'Neill, Comparisons of remote sensing retrievals and in situ measurements of aerosol fine mode fraction during ACE-Asia, *Geophys. Res. Lett.*, *33*, L05807, doi:10.1029/2005GL024926, 2006.
- Harder, J. W., J. W. Brault, P. V. Johnston, and G. H. Mount, Temperature dependent NO₂ cross sections at high spectral resolution, *J. Geophys. Res.*, *102*, 3861-3879, 1997.

- Huebert, B. J., T. Bates, P. B. Russell, G. Shi, Y. J. Kim, K. Kawamura, G. Carmichael, and T. Nakajima, An overview of ACE-Asia: Strategies for quantifying the relationships between Asian aerosols and their climatic impacts, *J. Geophys. Res.*, *108*(D23), 8633, doi:10.1029/2003JD003550, 2003.
- Ichoku, C., D. A. Chu, S. Mattoo, Y. J. Kaufman, L. A. Remer, D. Tanré, I. Slutsker, and B. Holben, A spatio-temporal approach for global validation and analysis of MODIS aerosol products, *Geophys. Res. Lett.*, *29*, 10.1029/2001GL013206, 2002.
- Ichoku, C., L. A. Remer, and T. F. Eck, Quantitative evaluation and intercomparison of morning and afternoon MODIS aerosol measurements from Terra and Aqua. *J. Geophys. Res.*, *110*, D10S03, doi: 10.1029/2004JD004987, 2005.
- Kahn, R., P. Banerjee, and D. McDonald, Sensitivity of multiangle imaging to natural mixtures of aerosols over ocean, *J. Geophys. Res.*, *106*, 18,219-18,238, 2001a.
- Kahn, R., P. Banerjee, D. McDonald, and J. Martonchik, Aerosol Properties Derived from Aircraft Multi-angle Imaging Over Monterey Bay, *J. Geophys. Res.* *106*, 11977-11995, 2001b.
- Kahn, R., J. Anderson, T.L. Anderson, T. Bates, F. Brechtel, C.M. Carrico, A. Clarke, S.J. Doherty, E. Dutton, R. Flagan, R. Frouin, H. Fukushima, B. Holben, S. Howell, B. Huebert, A. Jefferson, H. Jonsson, O. Kalashnikova, J. Kim, S-W. Kim, P. Kus, W-H. Li, J.M. Livingston, C. McNaughton, J. Merrill, S. Mukai, T. Murayama, T. Nakajima, P. Quinn, J. Redemann, M. Rood, P. Russell, I. Sano, B. Schmid, J. Seinfeld, N. Sugimoto, J. Wang, E.J. Welton, J-G. Won, S-C. Yoon, Environmental Snapshots From ACE-Asia, *J. Geophys. Res.*, Vol. 109, No. D19, D19S14 10.1029/2003JD004339, 2004.
- Kahn, R., B. Gaitley, J. Martonchik, D. Diner, K. Crean, and B. Holben, 2005, MISR global aerosol optical depth validation based on two years of coincident AERONET observations, *J. Geophys. Res.*, doi:10:1029/2004JD004706.
- Kahn et al., Aerosol Properties from MISR Space-based Multi-angle Imaging: INTEX-NA Campaign Validation and Results, *J. Geophys. Res.*, ICARTT special section, to be submitted 2006.
- Kalashnikova, O.V., R. Kahn, I.N. Sokolik, and W-H. Li, 2005, The ability of multi-angle remote sensing observations to identify and distinguish mineral dust types: Part 1. Optical models and retrievals of optically thick plumes, *J. Geophys. Res.*,doi: 10.1029/2004JD004550.

- Kaufman, Y. J., D. Tanré, L. A. Remer, E. Vermote, A. Chu, and B. N. Holben, Operational remote sensing of tropospheric aerosol over land from EOS moderate resolution imaging spectroradiometer, *J. Geophys. Res.*, *102*, 17,051-17,067, 1997.
- Kaufmann, Y.J., D. Tanré, and O. Boucher, A satellite view of aerosols in the climate system. *Nature*, *419*, 215-223, 2002.
- Levy, R. C., L. A. Remer, D. Tanré, Y. J. Kaufman, C. Ichoku, B. N. Holben, J. M. Livingston, P. B. Russell, and H. Maring, Evaluation of the Moderate-Resolution Imaging Spectroradiometer (MODIS) retrievals of dust aerosol over the ocean during PRIDE, *J. Geophys. Res.*, *108*(D19), 8594, doi:10.1029/2002JD002460, 2003.
- Livingston, J. M., P. B. Russell, J. S. Reid, J. Redemann, B. Schmid, D. Allen, O. Torres, R. C. Levy, L. A. Remer, B. N. Holben, A. Smirnov, O. Dubovik, E. J. Welton, J. Campbell, S. A. Christopher, J. Wang, Airborne sunphotometer measurements of aerosol optical depth and columnar water vapor during the Puerto Rico Dust Experiment, and comparison with land, aircraft, and satellite measurements, *J. Geophys. Res.*, *108* (D19), 8588, doi:10.1029/2002JD002520, 2003.
- Livingston et al., Comparison of Water Vapor Measurements by Airborne Sunphotometer and Near-Coincident In Situ and Satellite Sensors during INTEX-ITCT 2004, *J. Geophys. Res.*, ICARTT special section, to be submitted 2006.
- Martins, J. V., D. Tanré, L. Remer, Y. Kaufman, S. Mattoo and R. Levy, MODIS Cloud screening for remote sensing of aerosols over oceans using spatial variability. *Geophys. Res. Lett.*, **29**, 12, art. no.-1619, 2002.
- Martonchik, J.V., D.J. Diner, R. Kahn, M.M. Verstraete, B. Pinty, H.R. Gordon, and T.P. Ackerman, Techniques for the retrieval of aerosol properties over land and ocean using multiangle imaging, *IEEE Trans. Geosci. Remote Sens.*, *36*, 1212-1227, 1998.
- Martonchik, J.V., D.J. Diner, R.A. Kahn, B.J. Gaitley, and B.N. Holben, 2004, Comparison of MISR and AERONET aerosol optical depths over desert sites, *Geophys. Res. Lett.*, *31*, doi:10.1029/2004GL019807.
- McArthur, L. J. B., D. H. Halliwell, O. J. Niebergall, N. T. O'Neill, J. R. Slusser, and C. Wehrli, Field comparison of network Sun photometers, *J. Geophys. Res.*, *108*(D19), 4596, doi:10.1029/2002JD002964, 2003.

- Michalsky, J. J., J. C. Liljegren, and L. C. Harrison, A comparison of sun photometer derivations of total column water vapor and ozone to standard measures of same at the Southern Great Plains Atmospheric Radiation Measurement site, *J. Geophys. Res.*, *100*, 25,995-26,003, 1995.
- Pilewskie, P., O. Hofmann, B. Kindel, W. Gore, P. Russell, J. Livingston, J. Redemann, R. Bergstrom, S. Platnick, J. Daniel, T. Garrett, Cloud Properties Derived from Visible and Near-infrared Reflectance in the Presence of Aerosols, ICARTT JGR, in preparation, 2006.
- Ramanathan, V., P.J. Crutzen, J.T. Kiehl, and D. Rosenfeld, Aerosol, Climate and the Hydrological Cycle. *Science*, *294*, 2119-2124, 2001.
- Reagan, J., K. Thome, B. Herman, R. Stone, J. Deluisi, and J. Snider, A comparison of columnar water-vapor retrievals obtained with near-IR solar radiometer and microwave radiometer measurements, *J. Appl. Meteorol.*, *34*, 1384-1391, 1995.
- Redemann, J., P. B. Russell, and P. Hamill, Dependence of aerosol light absorption and single scattering albedo on ambient relative humidity for sulfate aerosols with black carbon cores, *J. Geophys. Res.*, *106*, 27485-27495, 2001.
- Redemann, J., S. Masonis, B. Schmid, T. Anderson, P. Russell, J. Livingston, O. Dubovik, A. Clarke, Clear-column closure studies of aerosols and water vapor aboard the NCAR C-130 in ACE-Asia, 2001, *J. Geophys. Res.* *108*(D23), 8655, doi:10.1029/2003JD003442, 2003.
- Redemann, J. P.B. Russell, R.W. Bergstrom, Aerosol-induced radiative flux changes in the Pacific Basin troposphere, *Eos Trans. AGU*, *85*(46), Fall Meet. Suppl., Abstract A11C-0080., 2004a.
- Redemann, J., A comparison of level-3 aerosol products from various sensors in the Pacific basin, MISR science team meeting, Pasadena, CA, Dec. 2004b.
- Redemann, J., B. Schmid, J. A. Eilers, R. A. Kahn, R. C. Levy, P. B. Russell, J. M. Livingston, P. V. Hobbs, W. L. Smith Jr., B. N. Holben, Suborbital measurements of spectral aerosol optical depth and its variability at sub-satellite grid scales in support of CLAMS, 2001, *J. Atmos. Sci.*, Vol. 62, No. 4, pp. 993-1007, 2005.
- Redemann, J., P. Pilewskie, P. Russell, J. Livingston, S. Howard, B. Schmid, J. Pommier, W. Gore, J. Eilers, and M. Wendisch, Airborne measurements of spectral direct aerosol radiative forcing in INTEX/ITCT, *J. Geophys. Res.*, accepted February 2006a.

- Redemann, J., Q. Zhang, B. Schmid, P. Russell, J. Livingston, L. Remer, H. Jonsson, Assessment of MODIS-derived visible and near-IR aerosol optical properties and their spatial variability in the presence of mineral dust, *Geophys. Res. Lett.*, to be submitted April 2006b.
- Reid, J. S., D. L. Westphal, J. M. Livingston, H. H. Jonsson, J. E. Kinney, E. J. Welton, A. A. Smirnov, M. Meier, D. L. Savoie, H. B. Maring, S. C. Tsay, S. Christopher, D. P. Eleuterio, and E. A. Reid, Measurements of Saharan dust by airborne and ground-based remote sensing methods during the Puerto Rico Dust Experiment (PRIDE), *J. Geophys. Res.*, in press, 2002.
- Remer, L. A., D. Tanré, Y. J. Kaufman, C. Ichoku, S. Mattoo, R. Levy, D. A. Chu, B. Holben, O. Dubovik, A. Smirnov, J. V. Martins, R. R. Li and Z. Ahmad, Validation of MODIS aerosol retrieval over ocean. *Geophys. Res. Lett.*, **29**, 12, art. no.-1618, 2002.
- Remer, L. A., Y. J. Kaufman, D. Tanre, S. Mattoo, D. A. Chu, J. V. Martins, R. R. Li, C. Ichoku, R. C. Levy, R. G. Kleidman, T. F. Eck, E. Vermote, and B. N. Holben, The MODIS aerosol algorithm, products and validation. *J. Atmos. Sci.*, **62**, 947-973, 2005.
- Remer, L. A. and Kaufman, Y. J.: Aerosol direct radiative effect at the top of the atmosphere over cloud free ocean derived from four years of MODIS data., *Atmos. Phys. Chem.*, **6**, 237-253, 2006.
- Rothman, L. S., Barbe, A., Benner, D. Chris, Brown, L. R., Camy-Peyret, C., Carleer, M. R., Chance, K., Clerbaux, C., Dana, V., Devi, V. M., Fayt, A., Flaud, J.-M., Gamache, R. R., Goldman, A., Jacquemart, D., Jucks, K. W., Lafferty, W. J., Mandin, J.-Y., Massie, S. T., Nemtchinov, V., Newnham, D. A., Perrin, A., Rinsland, C. P., Schroeder, J., Smith, K. M., Smith, M. A. H., Tang, K., Toth, R. A., Vander Auwera, J., Varanasi, P., and Yoshino, K.: The HITRAN molecular spectroscopic database: edition of 2000 including updates through 2001, *J. Quant. Spectr. & Rad. Transfer.*, **82**, 5-44, 2003.
- Russell, P. B., and J. Heintzenberg, An overview of the ACE 2 Clear Sky Column Closure Experiment (CLEARCOLUMN), *Tellus B* **52**, 463-483, 2000.
- Russell, P. B., J. M. Livingston, E. G. Dutton, R. F. Pueschel, J. A. Reagan, T. E. DeFoor, M. A. Box, D. Allen, P. Pilewskie, B. M. Herman, S. A. Kinne, and D. J. Hofmann, Pinatubo and pre-Pinatubo optical-depth spectra: Mauna Loa measurements, comparisons, inferred particle size distributions, radiative effects, and relationship to lidar data, *J. Geophys. Res.*, **98**, 22,969-22,985, 1993a.

- Russell, P. B., J. M. Livingston, R. F. Pueschel, J. A. Reagan, E. V. Browell, G. C. Toon, P. A. Newman, M. R. Schoeberl, L. R. Lait, L. Pfister, Q. Gao, and B. M. Herman, Post-Pinatubo optical depth spectra vs. latitude and vortex structure: Airborne tracking sunphotometer measurements in AASE II, *Geophys. Res. Lett.*, *20*, 2571-2574, 1993b.
- Russell, P. B., J. M. Livingston, R. F. Pueschel, J. J. Bauman, J. B. Pollack, S. L. Brooks, P. Hamill, L. W. Thomason, L. L. Stowe, T. Deshler, E. G. Dutton, and R. W. Bergstrom, Global to microscale evolution of the Pinatubo volcanic aerosol derived from diverse measurements and analyses, *J. Geophys. Res.*, *101*, 18,745-18,763, 1996.
- Schmid, B., and C. Wehrli, Comparison of sun photometer calibration by Langley technique and standard lamp, *Appl. Opt.*, *34*, 4500-4512, 1995.
- Schmid, B., K. J. Thome, P. Demoulin, R. Peter, C. Matzler, and J. Sekler, Comparison of modeled and empirical approaches for retrieving columnar water vapor from solar transmittance measurements in the 0.94- μm region, *J. Geophys. Res.*, *101*, 9345-9358, 1996.
- Schmid, B., P. R. Spyak, S. F. Biggar, C. Wehrli, J. Sekler, T. Ingold, C. Mätzler, and N. Kämpfer, Evaluation of the applicability of solar and lamp radiometric calibrations of a precision Sun photometer operating between 300 and 1025 nm, *Appl. Opt.*, *37*, 3923-3941, 1998.
- Schmid, B., Livingston, J. M., Russell, P. B., Durkee, P. A., Collins, D. R., Flagan, R. C., Seinfeld, J. H., Gasso, S., Hegg, D. A., Ostrom, E., Noone, K. J., Welton, E. J., Voss, K., Gordon, H. R., Formenti, P., and Andreae, M. O. Clear sky closure studies of lower tropospheric aerosol and water vapor during ACE 2 using airborne sunphotometer, airborne in-situ, space-borne, and ground-based measurements. *Tellus B* *52*, 568-593, 2000.
- Schmid, B., J. J. Michalsky, D. W. Slater, J. C. Barnard, R. N. Hathore, J. C. Liljegren, B. N. Holben, T. F. Eck, J. M. Livingston, P. B. Russell, T. Ingold, and I. Slutsker, Comparison of columnar water-vapor measurements from solar transmittance methods, *Appl. Opt.*, *40*, 1886-1896, 2001.
- Schmid, B., J. Redemann, P. B. Russell, P. V. Hobbs, D. L. Hlavka, M. J. McGill, B. N. Holben, E. J. Welton, J. R. Campbell, O. Torres, R. A. Kahn, D. J. Diner, M. C. Helmlinger, D. A. Chu, C. Robles-Gonzalez, and G. De Leeuw, Coordinated airborne, spaceborne, and ground-based measurements of massive, thick aerosol layers during the dry season in Southern Africa, *J. Geophys. Res.*, *108* (D13), 8496, doi:10.1029/2002JD002297, 2003a.

- Schmid, B., D. A. Hegg, J. Wang, D. Bates, J. Redemann, P. B. Russell, J. M. Livingston, H. H. Jonsson, E. J. Welton, J. H. Seinfeld, R. C. Flagan, D. S. Covert, O. Dubovik, A. Jefferson, Column closure studies of lower tropospheric aerosol and water vapor during ACE-Asia using airborne sunphotometer, airborne in-situ and ship-based lidar measurements, *J. Geophys. Res.* 108 (D23), 8656, doi:10.1029/2002JD003361, 2003b.
- Schmid B., R. Ferrare, C. Flynn, R. Elleman, D. Covert, A. Strawa, E. Welton, D. Turner, H. Jonsson, J. Redemann, J. Eilers, K. Ricci, A. G. Hallar, M. Clayton, J. Michalsky, A. Smirnov, B. Holben, J. Barnard. How well do state-of-the-art techniques measuring the vertical profile of tropospheric aerosol extinction compare? *J. Geophys. Res.* Vol. 111, D05S07, doi:10.1029/2005JD005837, 2006.
- Singh, H. B., W. H. Brune, J. H. Crawford, and D. J. Jacob, Overview of the Summer 2004 Intercontinental Chemical Transport Experiment-North America (INTEX-A), *J. Geophys. Res.*, INTEX-A special section, submitted 2006.
- Smith Jr., W.L., Charlock, T.P., Kahn, R., Martins, J.V., Remer, L.A., Hobbs, P.V., Redemann, J., Rutledge, C.K., EOS-TERRA aerosol and radiative flux validation: An overview of the Chesapeake Lighthouse and Aircraft Measurements for Satellites (CLAMS) experiment, *J. Atmos. Sci.*, doi: 10.1175/JAS3398.1, Vol. 62, No. 4, pp. 903-918, 2005.
- Tanre', D., Y. J. Kaufman, M. Herman, and S. Matto (1997), Remote sensing of aerosol properties over oceans using the MODIS/EOS spectral radiance, *J. Geophys. Res.*, 102, 16,971 – 16,988.
- Wang, W., M.J. Rood, C.M. Carrico, D.S. Covert, P.K. Quinn, T.S. Bates, and T. Baynard (2006) Aerosol Optical Properties over the Northwestern Atlantic Ocean during NEAQS-ITCT 2004, and the Influence of Particulate Organic Matter on Aerosol Hygroscopicity, *J. Geophys. Res.*, ICARTT special section, to be submitted 2006.
- Wen, G. Y., Marshak, A. and Cahalan, R. F.: Impact of 3-D clouds on clear-sky reflectance and aerosol retrieval in a biomass burning region of Brazil., *IEEE Geosci Rem. Sens. Lett.*, 3 (1), 169-172, 2006.
- Tanré, D., Remer, L. A., Kaufman, Y. J., Mattoo, S., Hobbs, P. V., Livingston, J. M., Russell, P. B. and Smirnov, A.: Retrieval of aerosol optical thickness and size distribution over ocean from the MODIS Airborne Simulator during TARFOX, *J. Geophys. Res.*, 104, 2261-2278, 1999.

RUSSELL ET AL.: MULTI-GRID-CELL SATELLITE VALIDATION

P. B. Russell, J. Eilers, NASA Ames Research Center, MS 245-5, Moffett Field, CA 94035-1000, USA. (Philip.B.Russell@nasa.gov, James.A.Eilers@nasa.gov)

J. M. Livingston, SRI International, 333 Ravenswood Avenue, Menlo Park, CA 94025, USA. (jlivingston@mail.arc.nasa.gov)

S. A. Ramirez, J. Redemann and B. Schmid, Bay Area Environmental Research Institute, 560 3rd Street West, Sonoma, CA 95476, USA. (s.a.ramirez@mail.arc.nasa.gov, jredemann@mail.arc.nasa.gov, bschmid@mail.arc.nasa.gov)

A. Chu, NASA Goddard Space Flight Center, Laboratory for Atmospheres , Code 912, Greenbelt, MD 20771, USA. (achu@climate.gsfc.nasa.gov)

R. A. Kahn, MS. 169-237, Jet Propulsion Lab, 4800 Oak Grove Dr., Pasadena, CA 91109-8099 (ralph.kahn@jpl.nasa.gov)

P. K. Quinn, NOAA/PMEL OCRD, 7600 Sandpoint Way NE, Seattle, WA 98115 (Patricia.K.Quinn@noaa.gov)

M. J. Rood, W. Wang, Env. Eng. & Sci., 3213 NCEL/MC-250, 205 N. Mathews Ave, Dept. of Civil & Environ. Eng., University of Illinois at Urbana-Champaign, Urbana, IL USA 61801-2352 (m-rood@uiuc.edu)

Tables

Table 1: Ratio of AOD below to above the J31

wavelength (nm)	450	500	550	700
range, %	1.0-13.1	1.0-13.9	1.0-15.4	1.0-13.1
mean, %	6.1	6.2	6.3	5.9
st_dev, %	4.5	4.8	5.4	4.7

Figure Captions

1. Comparison of AOD(500 nm) below J31 (estimated from measurements of humidified scattering and absorption made on the ship Ron Brown), above J31 (from AATS measurements), above the Ron Brown (from 2 handheld sunphotometers, RB 3803 and RB 5355), and below satellites (from MODIS and MISR retrievals). Numbers below date labels give time (in decimal hours UT) of each measurement.
2. AOD spectra for the cases in Figure 1. AATS AODs shown are as measured, i.e., describing the column above the J31; with no estimate of AOD below the J31 added. Note different AOD scales in middle row to accommodate large AODs on 22 and 29 July.
3. **Left frame:** MISR image from camera Aa, Level 1B2 RGB, 1534 UT (15.57 UT in decimal hours) on 29 July 2004. Orbit 24542, 1.1 km resolution. **Right frame:** J31 flight track, with location at satellite overpass time marked.
4. **Top frame:** J31 flight path at minimum altitude with superimposed MISR grid cells. Gaps indicate clouds are impacting AATS's view of the sun, or the J31 altitude exceeds 100 m (which typically occurred during J31 turns). **Bottom frame:** AATS-measured multiwavelength AOD along the flight path, showing edges of MISR grid cells and flight direction.
5. Comparison of AOD spectra measured by AATS and MISR (Version 15), 29 July 2004. Colors of MISR spectra match the MISR grid cell colors in Figure 4. The AATS spectrum (open black circles) is a mean from the whole flight path of Figure 4, along with the typical AATS measurement uncertainty (narrow ticks), standard deviation of results along the flight path (wide ticks), and range along the flight path (vertical bars).
6. As in Figure 5, but for MISR Version 16.
7. Scatter plots comparing AATS and MISR Version 15 AOD for 29 July 2004.
8. Scatter plots comparing AATS and MISR Version 16 AOD for 29 July 2004.

9. **Left frame:** MODIS Aqua image, 21 July 2004, 1805 UT. **Right frame:** J31 flight track.
10. J31 flight path on 21 July 2004, with MODIS grid cells superimposed on path parts at minimum altitude (<100 m ASL).
11. Vertical profiles of AOD and extinction from AATS measurements on the J31. **Left 2 frames:** from initial ascent out of Pease. **Right 2 frames:** from spiral descent 1.
12. **Left frame:** Detail of J31 flight path on 21 July 2004, showing MODIS grid cells. **Right frames:** AOD, CWV, and J31 altitude vs. time along the flight path at left. Vertical lines in top right frame show edges of MODIS grid cells.
13. Comparison of AOD spectra from J31 and MODIS within the grid cells shown in Figure 12.
14. Comparisons of MODIS and AATS AOD-vs.-wavelength spectra for each of the 13 MODIS grid cells along the 21 July 2004 J31 path shown in Figure 12.
15. Scatter plots comparing AATS and MODIS-Aqua AOD for the 21 July 2004 case. Blue lines show the MODIS over-ocean uncertainty estimates, $\Delta\tau = \pm 0.03 \pm 0.05\tau$. **Left frame:** including all 13 grid cells. **Right frame:** excluding the blue grid cell in Figure 12 (blue spectrum in Figure 13), data points for which were indicated in the left frame with blue boxes.
16. Scatter plots comparing AATS and MODIS AOD for all coincidences with good data in INTEX-ICARTT 2004. Blue lines show the MODIS over-ocean uncertainty estimates, $\Delta\tau = \pm 0.03 \pm 0.05\tau$. **Left frame:** MODIS-Aqua vs. AATS. **Right frame:** MODIS-Terra vs. AATS.
17. Scatter plot comparisons of 553-855 nm (blue symbols) and 855-2119 nm (red symbols) Ångstrom exponents for MODIS-Terra (crosses) and MODIS-Aqua (triangles) versus

AATS-14 derived Ångstrom exponents. **Left frame:** All 40 Aqua and 17 Terra cases.

Right frame: Excluding all cases with AATS AOD(855)<0.1.

18. MODIS-AATS differences in Ångstrom exponents plotted vs. AATS AOD(855 nm).
19. Comparison of AATS and MODIS AOD spectra and Ångstrom exponent values for 15 MODIS-Aqua grid cells of the 17.90 UT Aqua overpass on 8 August 2004.
20. Fields of AOD retrieved from MODIS for 29 July 2004 with the glint mask reduced to 25°. **Left frame:** MODIS-Terra, 1535 UT. **Right frame:** MODIS-Aqua, 1715 UT.
21. J31 flight path on 29 July 2004, underflying both Terra (1534 UT) and Aqua at or near minimum altitude (60 to 100 m).
22. Comparison of AATS and MODIS-Terra AOD spectra for the 29 July 2004 1534 UT Terra overpass. Inset shows 16 MODIS grid cells that yielded AOD retrievals along the J31 low-altitude path. Resulting AOD spectra are color coded by grid cell color. The AATS spectrum (open black circles) is a mean from the whole low-altitude flight path shown, along with the typical AATS measurement uncertainty (narrow ticks), standard deviation of results along the flight path (wide ticks), and range along the flight path (vertical bars).
23. As in Figure 22, but for AATS and MODIS-Aqua AOD spectra for the 29 July 2004 1710 UT Aqua overpass, corresponding J31 low-altitude path, and 6 corresponding grid cells.

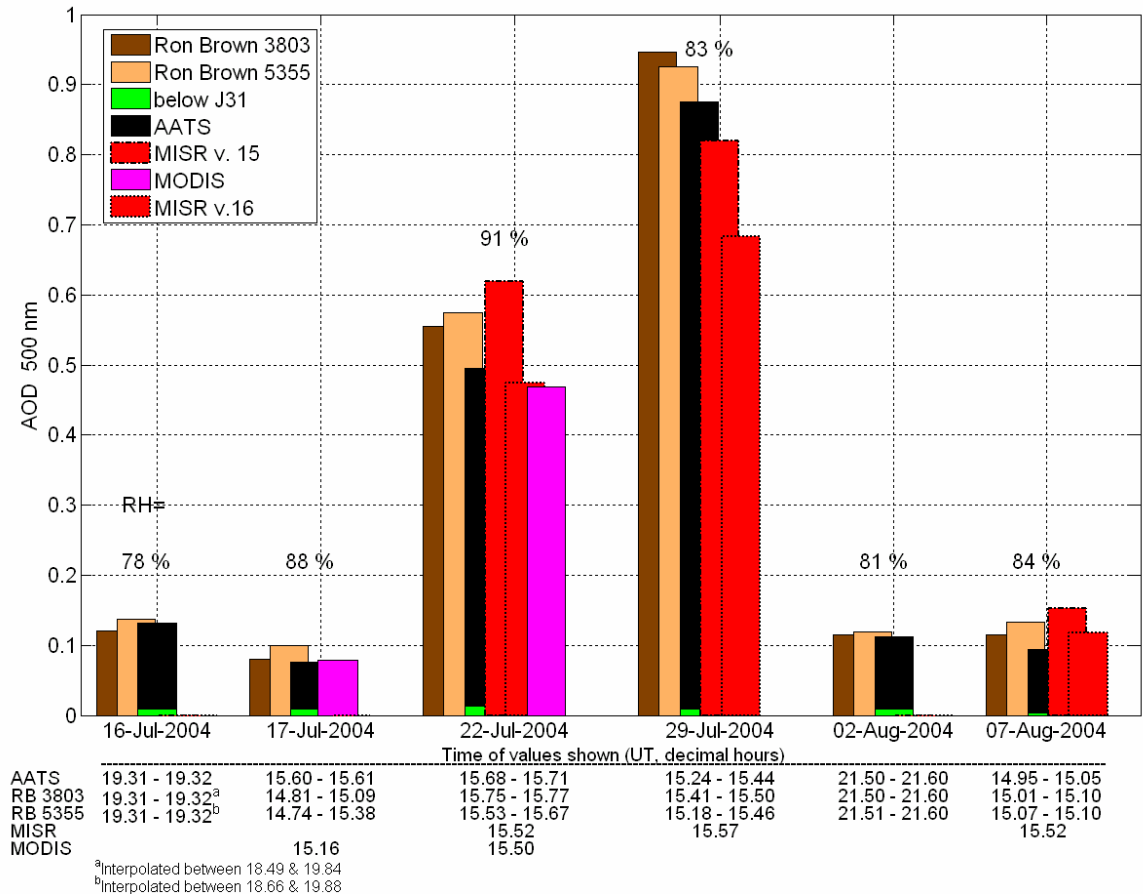


Figure 1. Comparison of AOD(500 nm) below J31 (estimated from measurements of humidified scattering and absorption made on the ship Ron Brown), above J31 (from AATS measurements), above the Ron Brown (from 2 handheld sunphotometers, RB 3803 and RB 5355), and below satellites (from MODIS and MISR retrievals). Numbers below date labels give time (in decimal hours UT) of each measurement.

RUSSELL ET AL.: MULTI-GRID-CELL SATELLITE VALIDATION

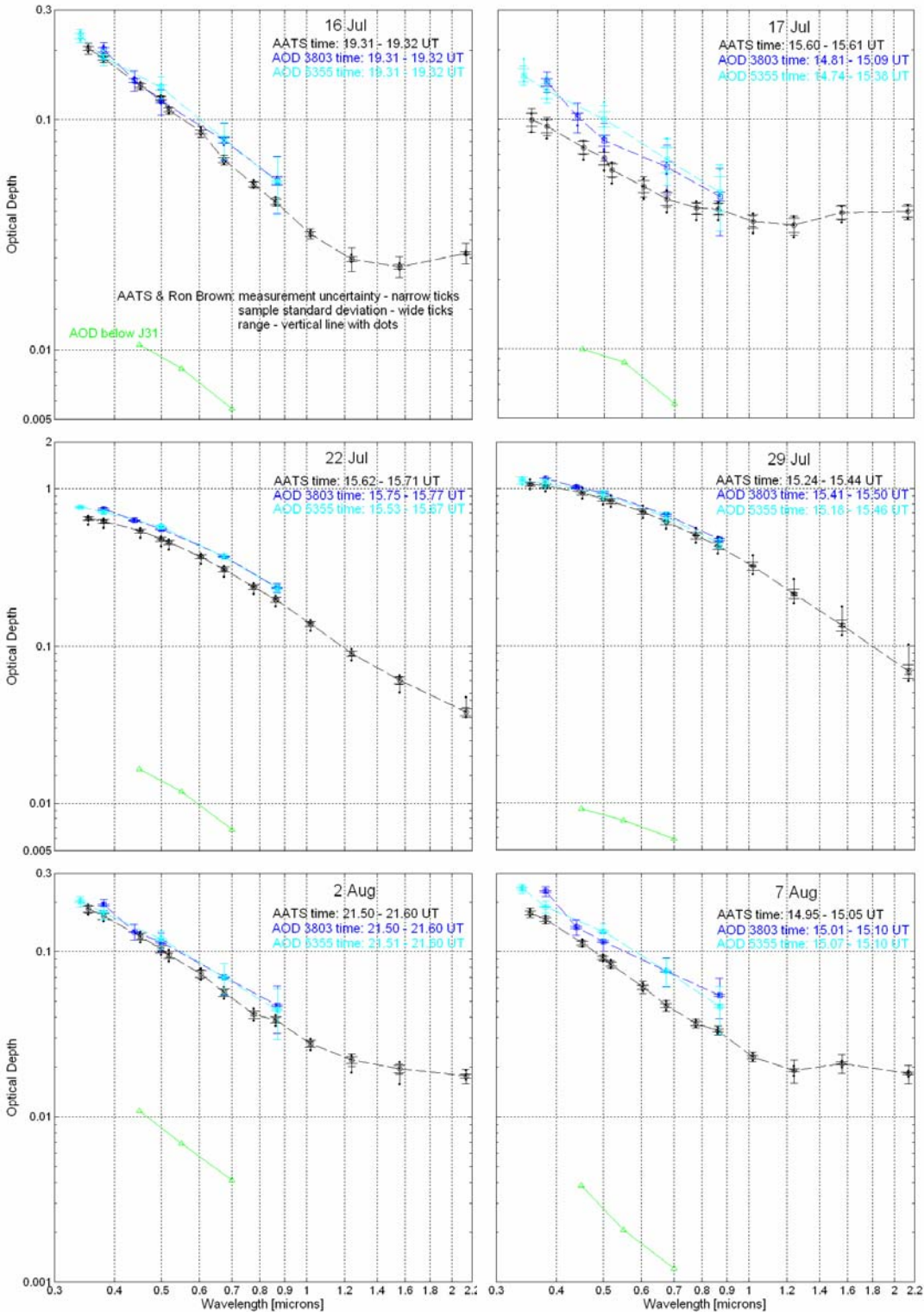
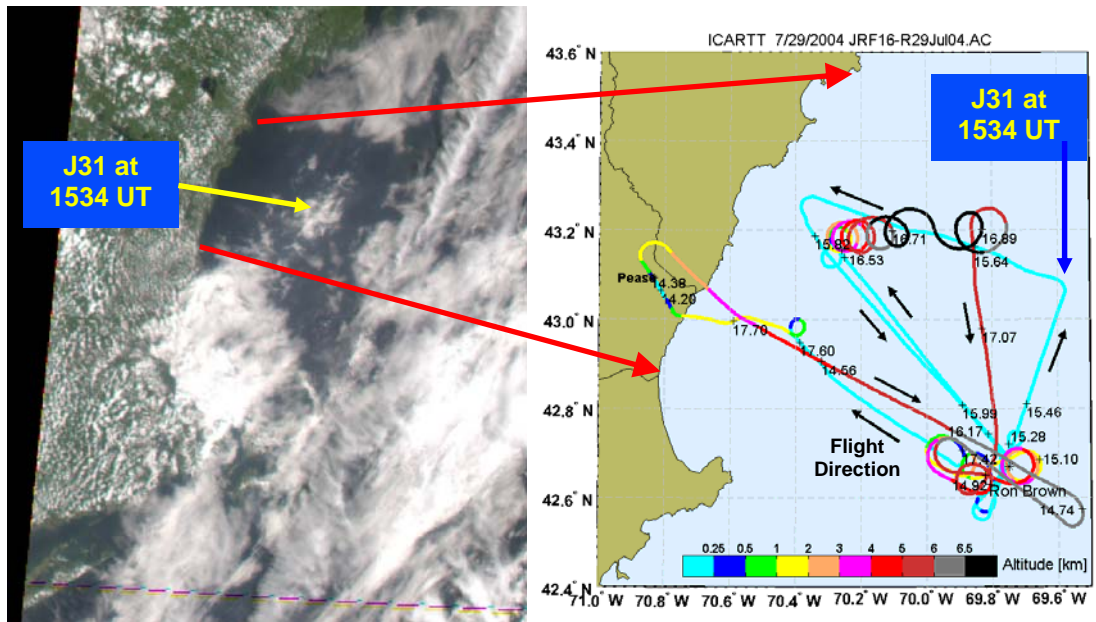


Figure 2. AOD spectra for the cases in Figure 1. AATS AODs shown are as measured, i.e., describing the column above the J31; with no estimate of AOD below the J31 added. Note different AOD scales in middle row to accommodate large AODs on 22 and 29 July.



Jetstream-31 Flight Track

Figure 3. Left frame: MISR image from camera Aa, Level 1B2 RGB, 1534 UT (15.57 UT in decimal hours) on 29 July 2004. Orbit 24542, 1.1 km resolution. **Right frame:** J31 flight track, with location at satellite overpass time marked.

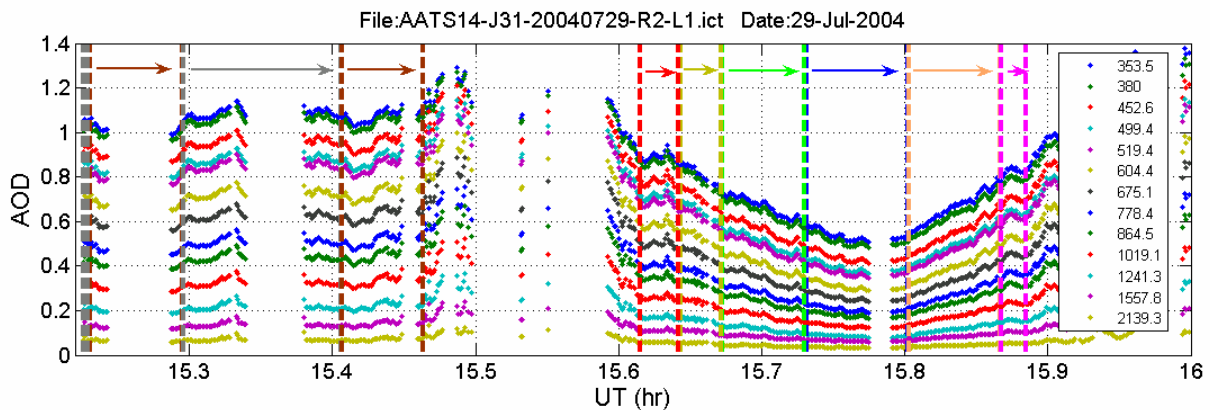
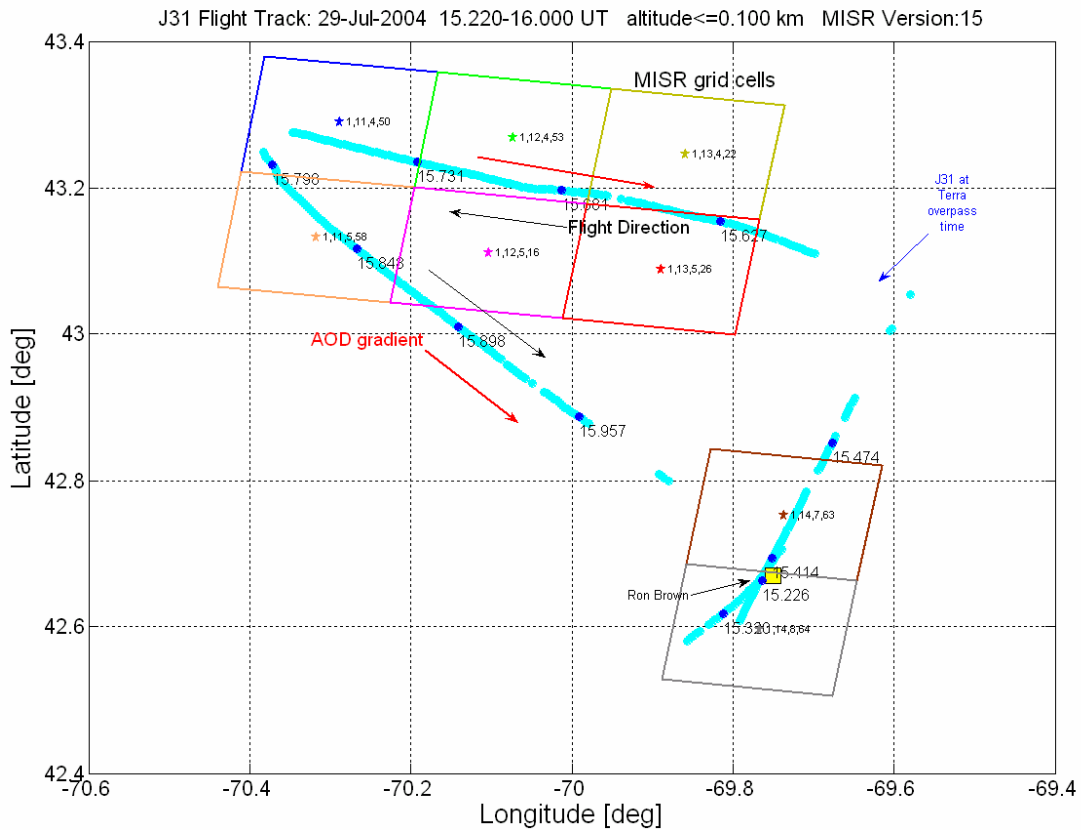


Figure 4. Top frame: J31 flight path at minimum altitude with superimposed MISR grid cells. Gaps indicate clouds are impacting AATS’s view of the sun, or the J31 altitude exceeds 100 m (which typically occurred during J31 turns). **Bottom frame:** AATS-measured multiwavelength AOD along the flight path, showing edges of MISR grid cells and flight direction.

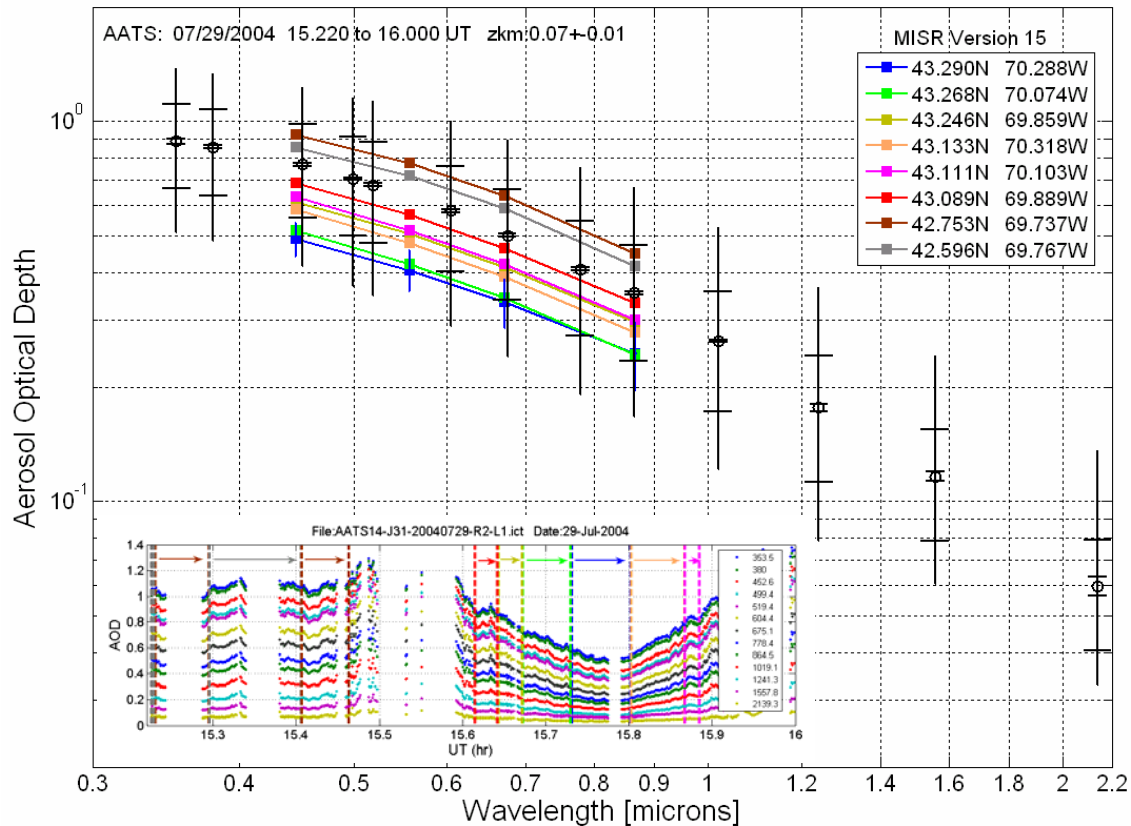


Figure 5. Comparison of AOD spectra measured by AATS and MISR (Version 15), 29 July 2004. Colors of MISR spectra match the MISR grid cell colors in Figure 4. The AATS spectrum (open black circles) is a mean from the whole flight path of Figure 4, along with the typical AATS measurement uncertainty (narrow ticks), standard deviation of results along the flight path (wide ticks), and range along the flight path (vertical bars).

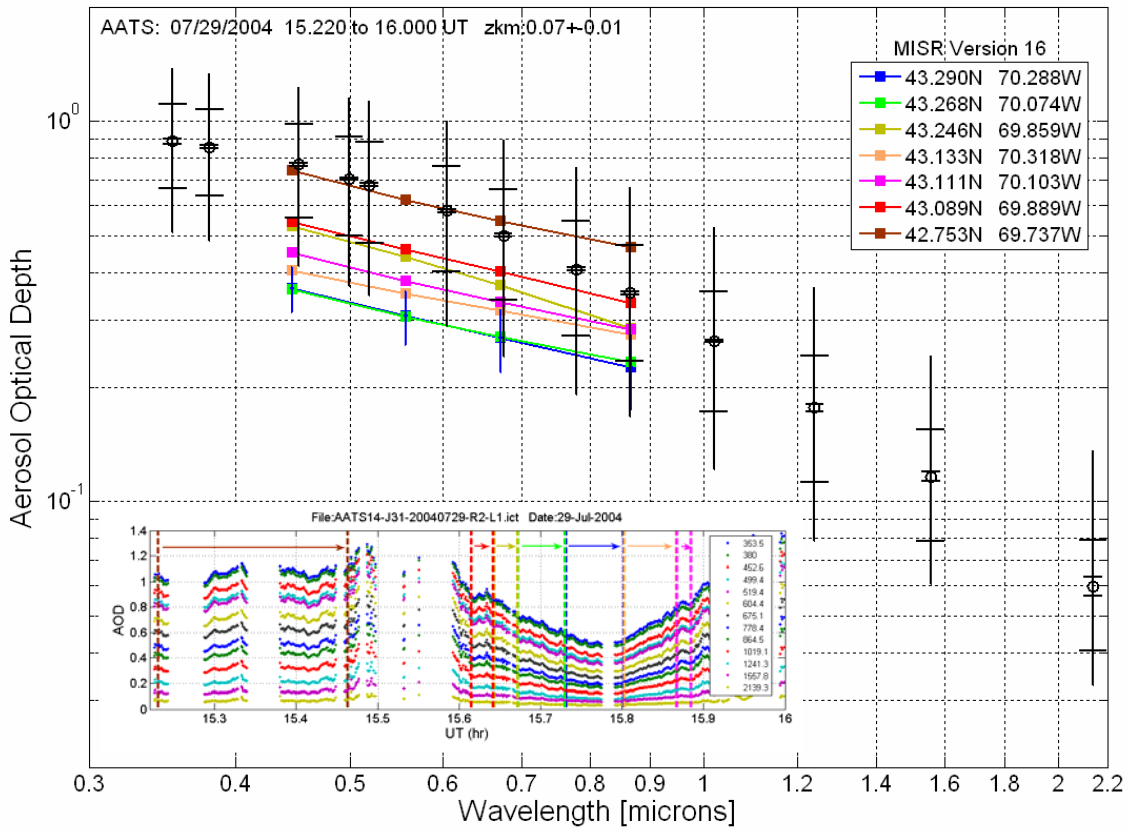


Figure 6. As in Figure 5, but for MISR Version 16.

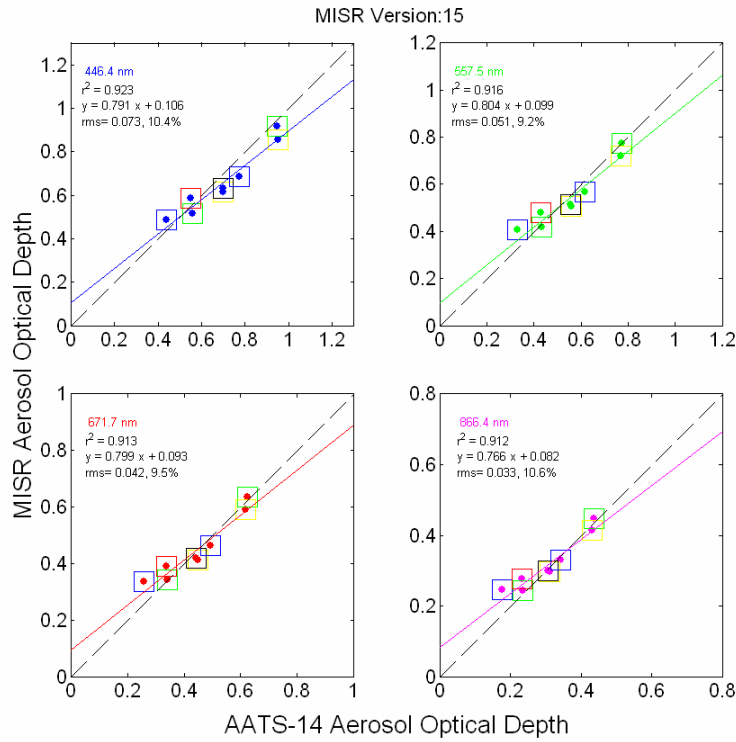


Figure 7. Scatter plots comparing AATS and MISR Version 15 AOD for 29 July 2004.

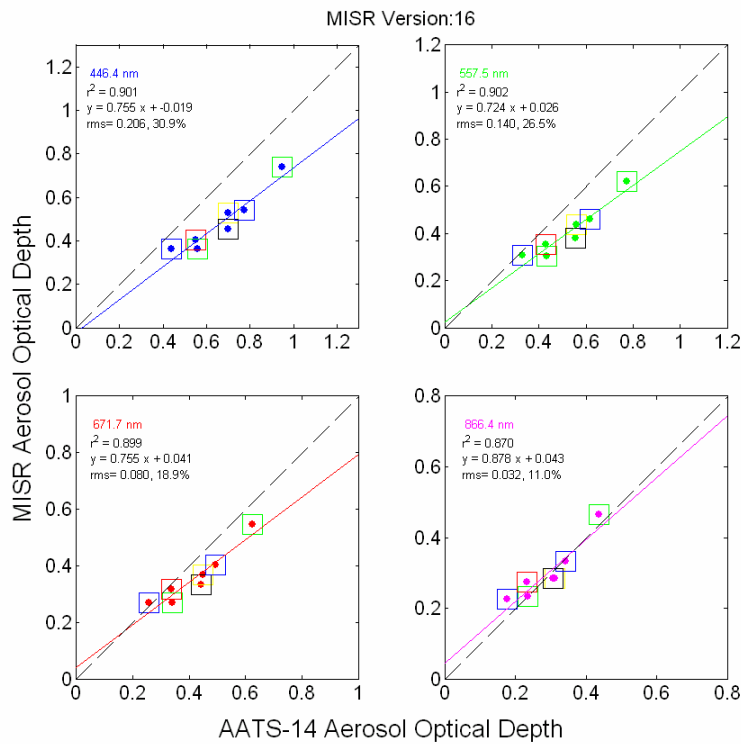


Figure 8. Scatter plots comparing AATS and MISR Version 16 AOD for 29 July 2004.

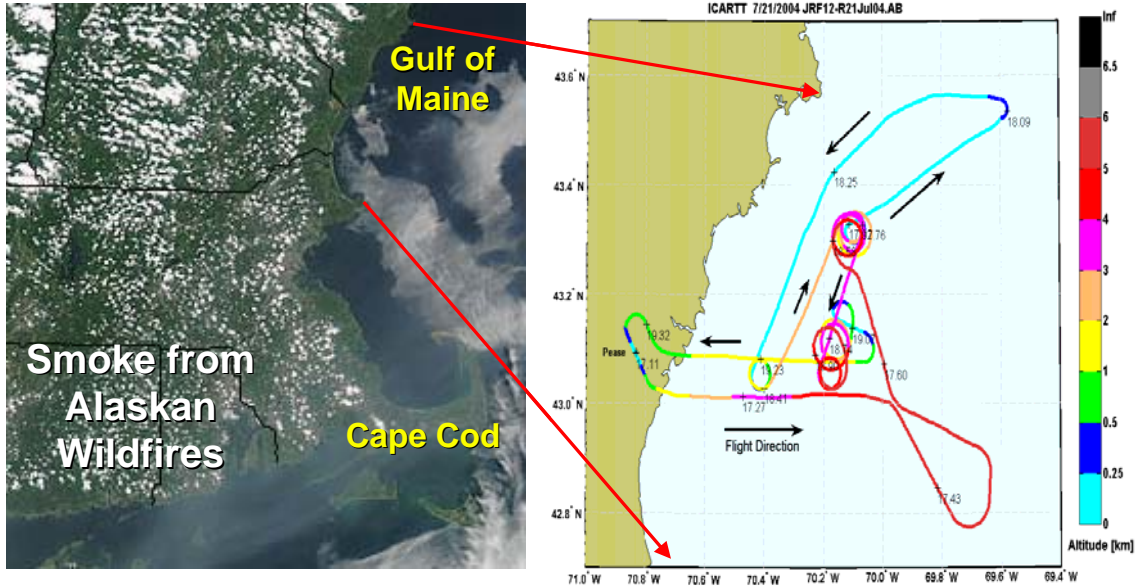


Figure 9. **Left frame:** MODIS Aqua image, 21 July 2004, 1805 UT. **Right frame:** J31 flight track.

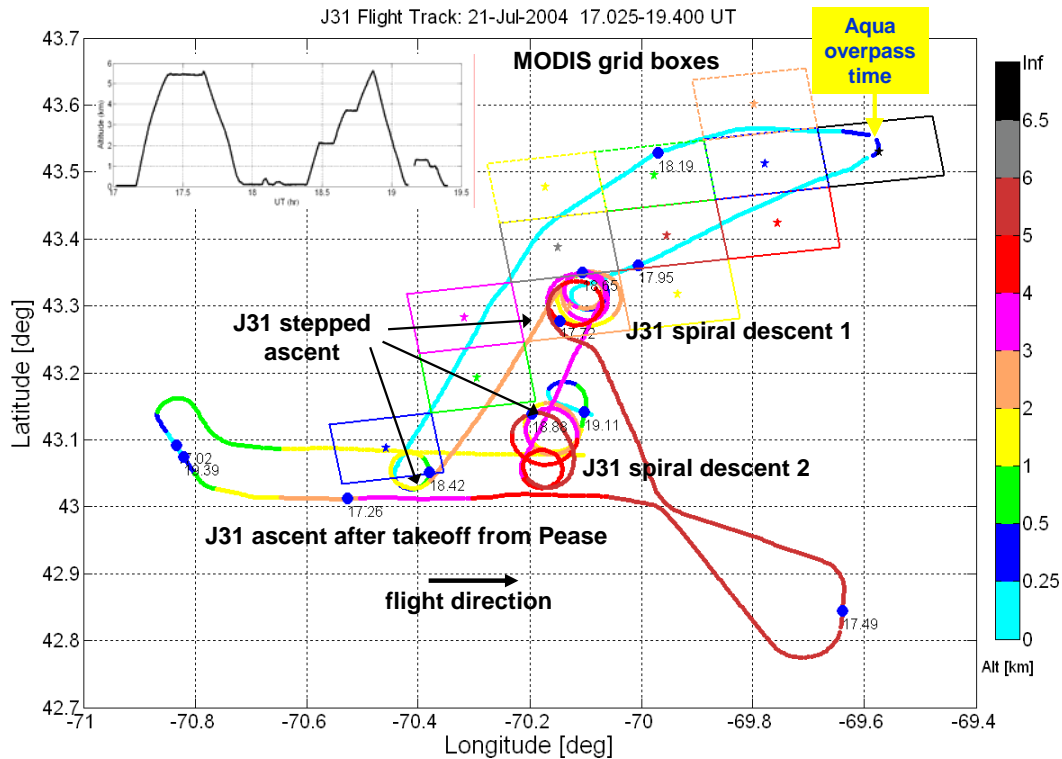


Figure 10. J31 flight path on 21 July 2004, with MODIS grid cells superimposed on path parts at minimum altitude (<100 m ASL).

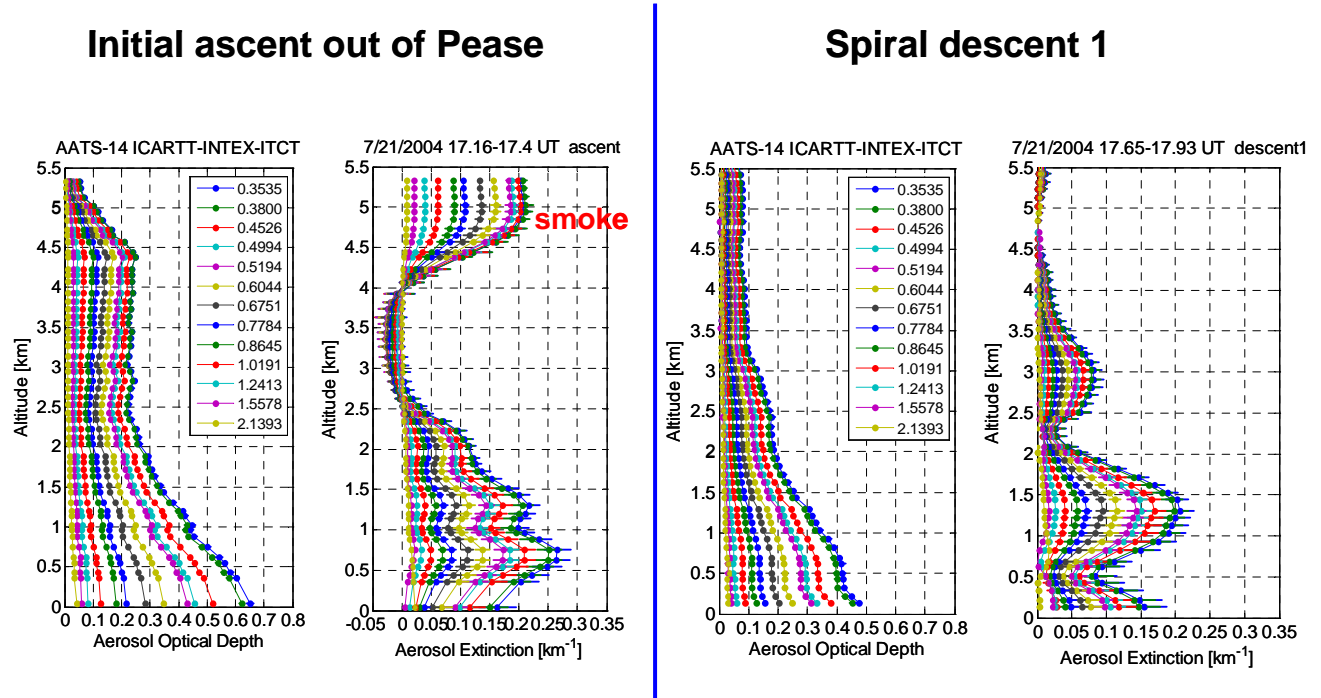


Figure 11. Vertical profiles of AOD and extinction from AATS measurements on the J31. **Left 2 frames:** from initial ascent out of Pease. **Right 2 frames:** from spiral descent 1.

RUSSELL ET AL.: MULTI-GRID-CELL SATELLITE VALIDATION

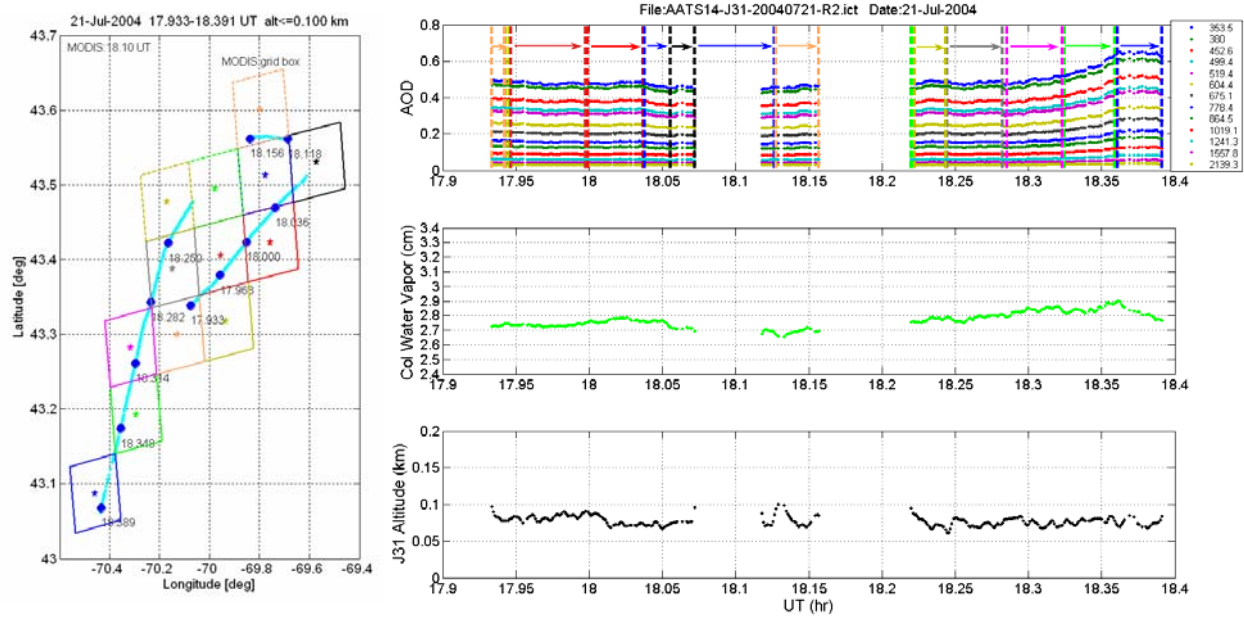


Figure 12. **Left frame:** Detail of J31 flight path on 21 July 2004, showing MODIS grid cells.

Right frames: AOD, CWV, and J31 altitude vs time along the flight path at left. Vertical lines in top right frame show edges of MODIS grid cells.

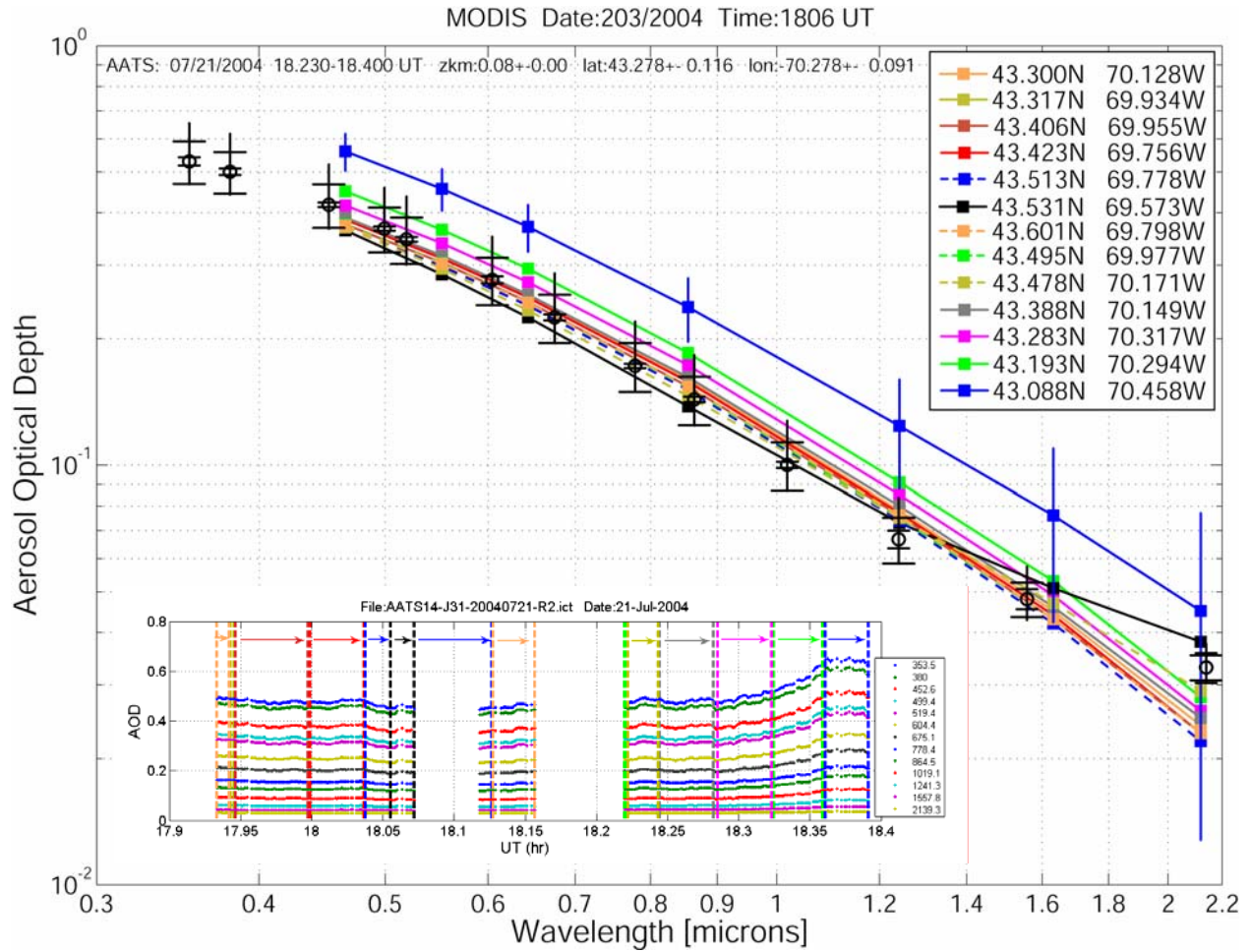


Figure 13. Comparison of AOD spectra from J31 and MODIS within the grid cells shown in Figure 12.

RUSSELL ET AL.: MULTI-GRID-CELL SATELLITE VALIDATION

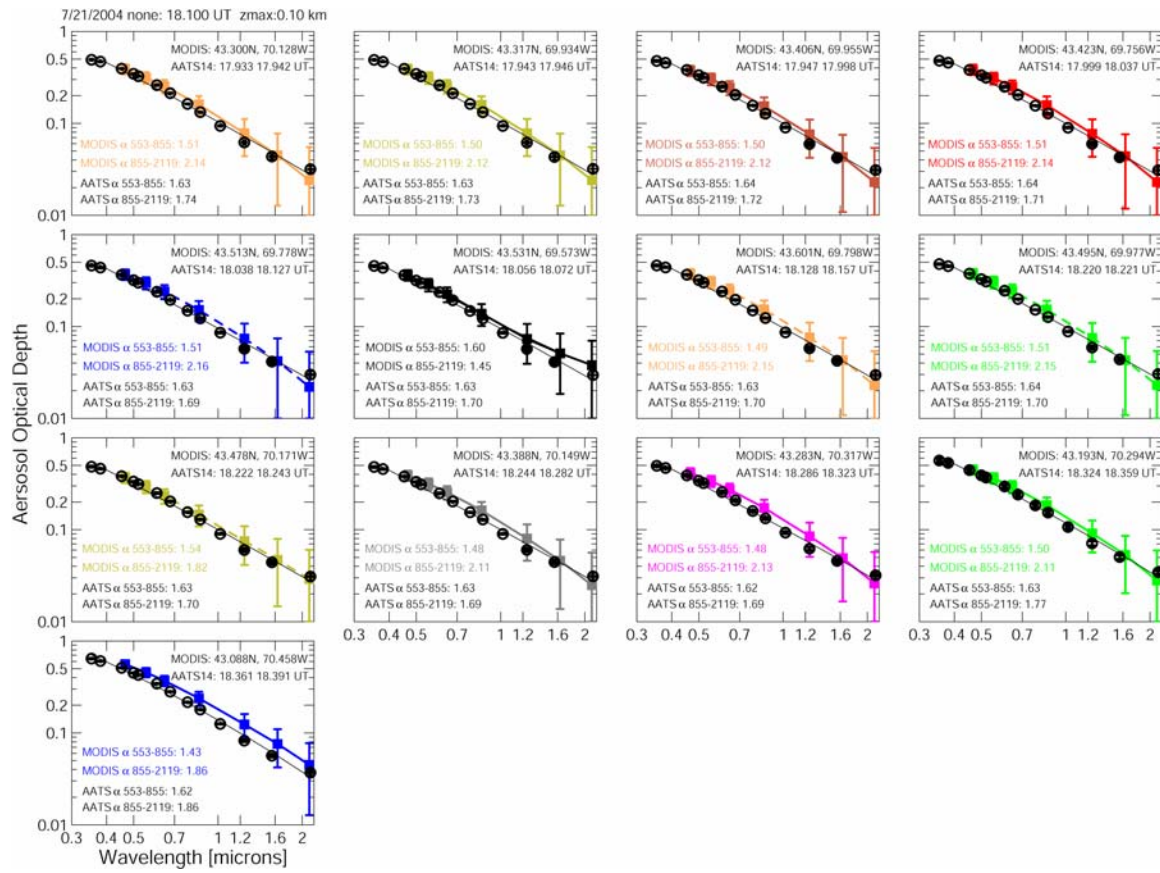


Figure 14. Comparisons of MODIS and AATS AOD-vs-wavelength spectra for each of the 13 MODIS grid cells along the 21 July 2004 J31 path shown in Figure 12.

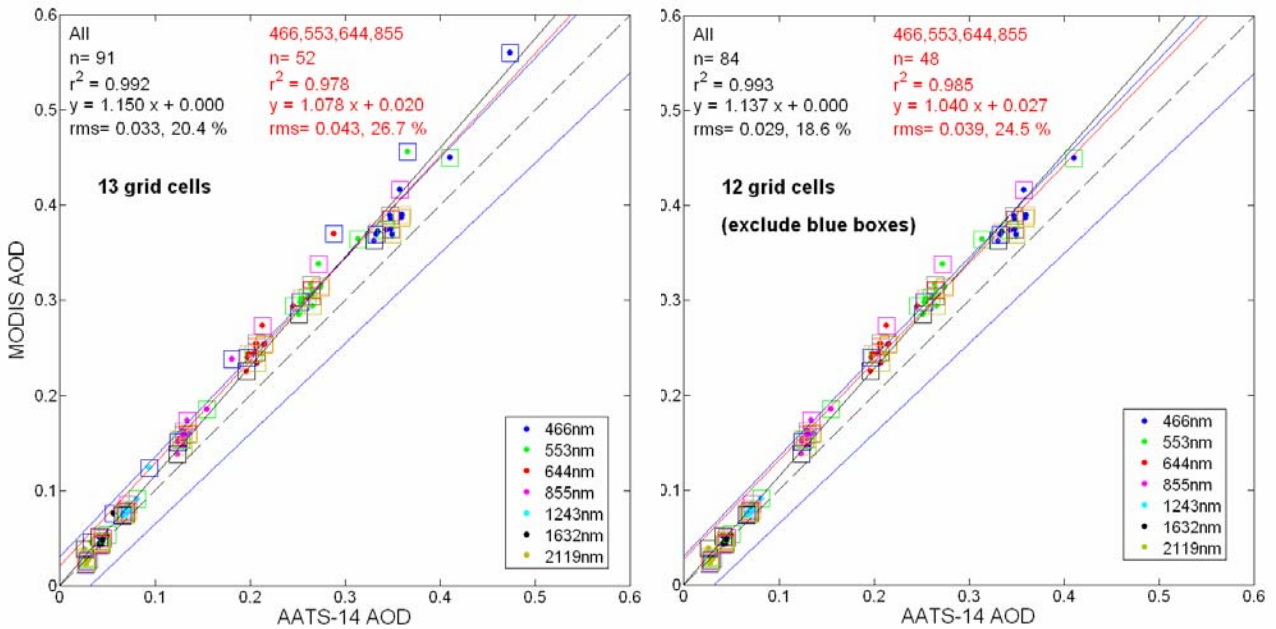


Figure 15. Scatter plots comparing AATS and MODIS-Aqua AOD for the 21 July 2004 case.

Blue lines show the MODIS over-ocean uncertainty estimates, $\Delta\tau = \pm 0.03 \pm 0.05\tau$. **Left frame:** including all 13 grid cells. **Right frame:** excluding the blue grid cell in Figure 12 (blue spectrum in Figure 13), data points for which were indicated in the left frame with blue boxes.

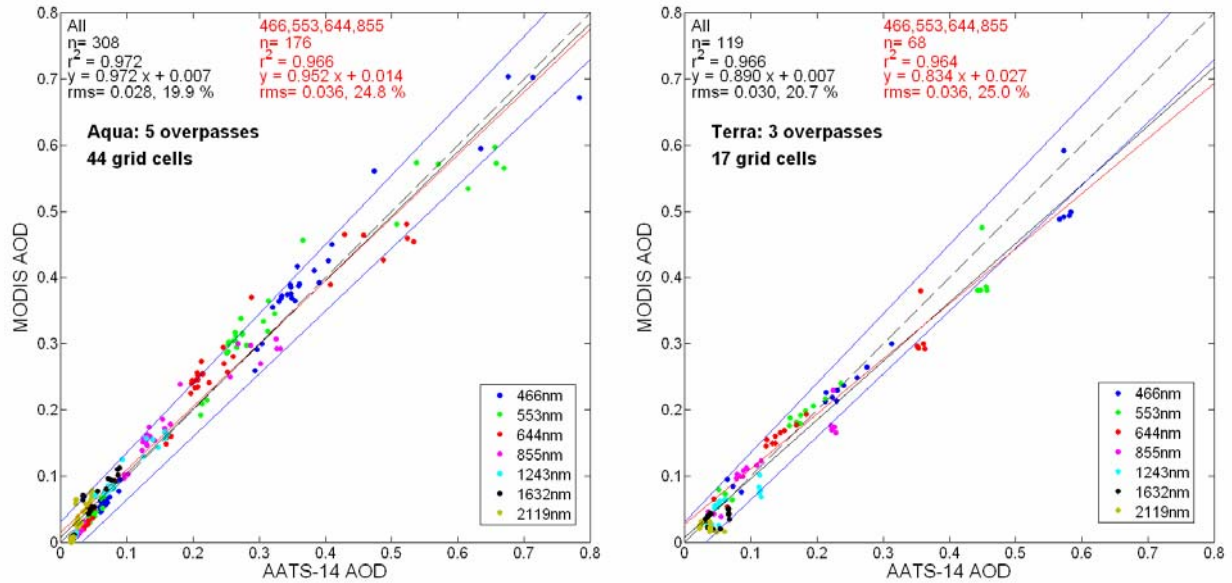


Figure 16. Scatter plots comparing AATS and MODIS AOD for all coincidences with good data in INTEX-ICARTT 2004. Blue lines show the MODIS over-ocean uncertainty estimates, $\Delta\tau = \pm 0.03 \pm 0.05\tau$. **Left frame:** MODIS-Aqua vs AATS. **Right frame:** MODIS-Terra vs. AATS.

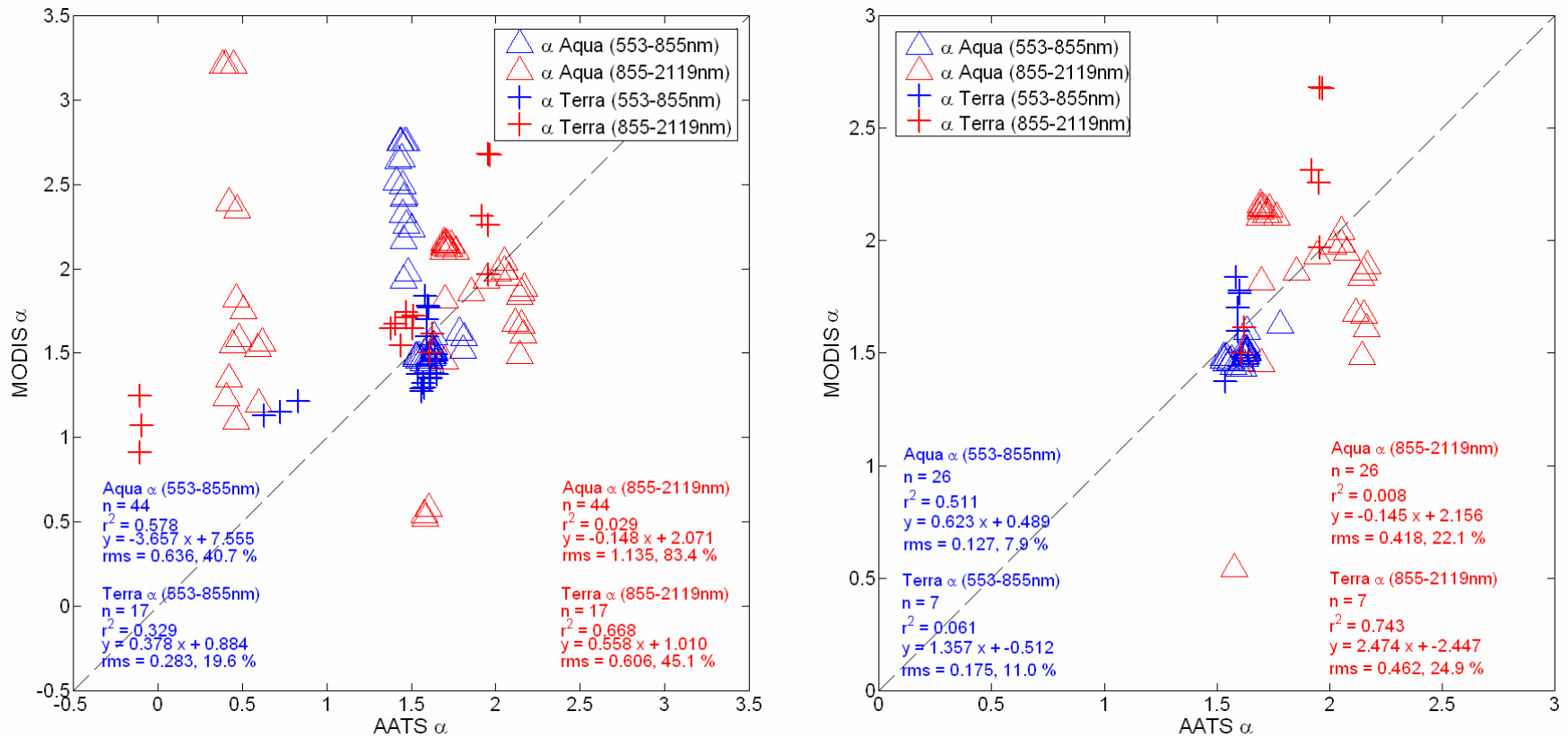


Figure 17. Scatter plot comparisons of 553-855 nm (blue symbols) and 855-2119 nm (red symbols) Ångstrom exponents for MODIS-Terra (crosses) and MODIS-Aqua (triangles) versus AATS-14 derived Ångstrom exponents. **Left frame:** All 40 Aqua and 17 Terra cases. **Right frame:** Excluding all cases with AATS AOD(855)<0.1.

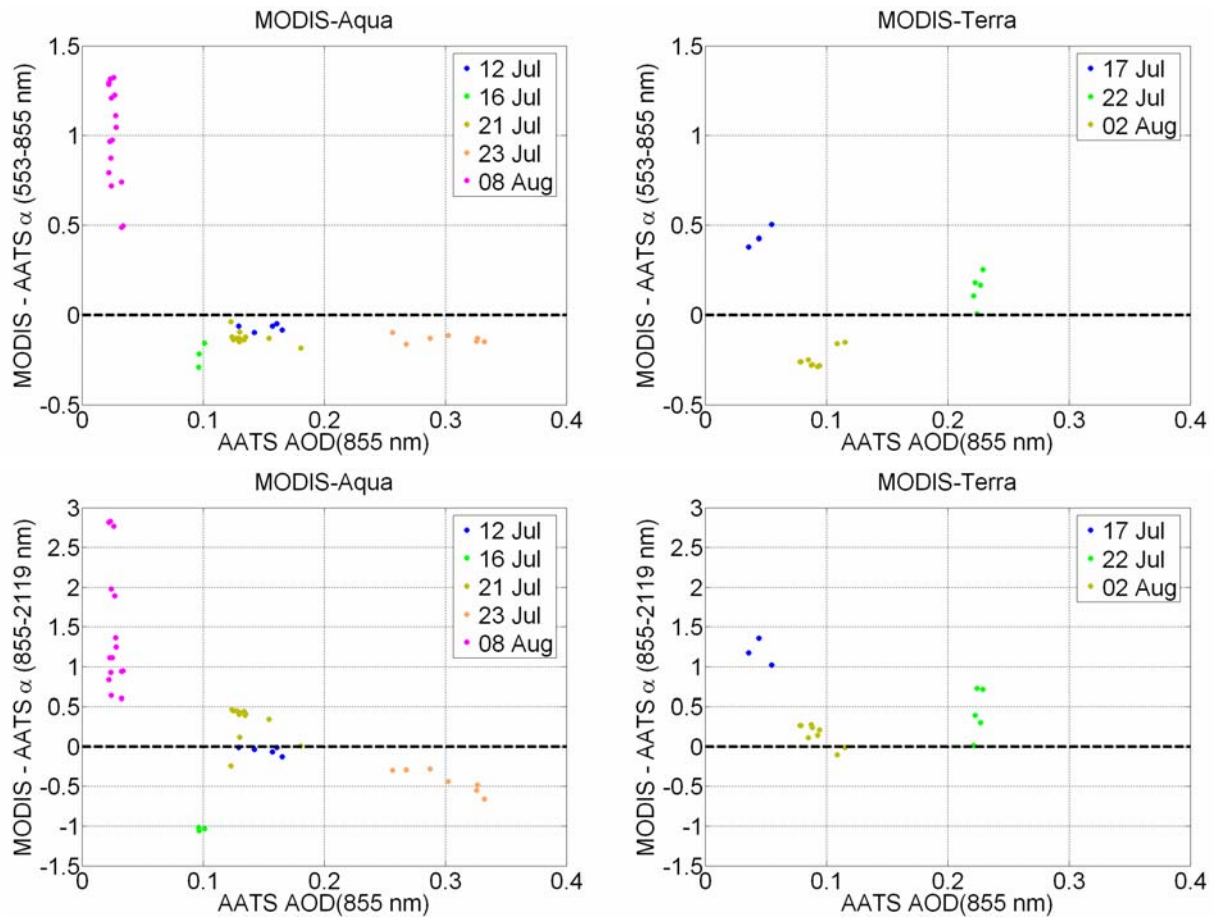


Figure 18. MODIS-AATS differences in Ångstrom exponents plotted vs AATS AOD(855 nm).

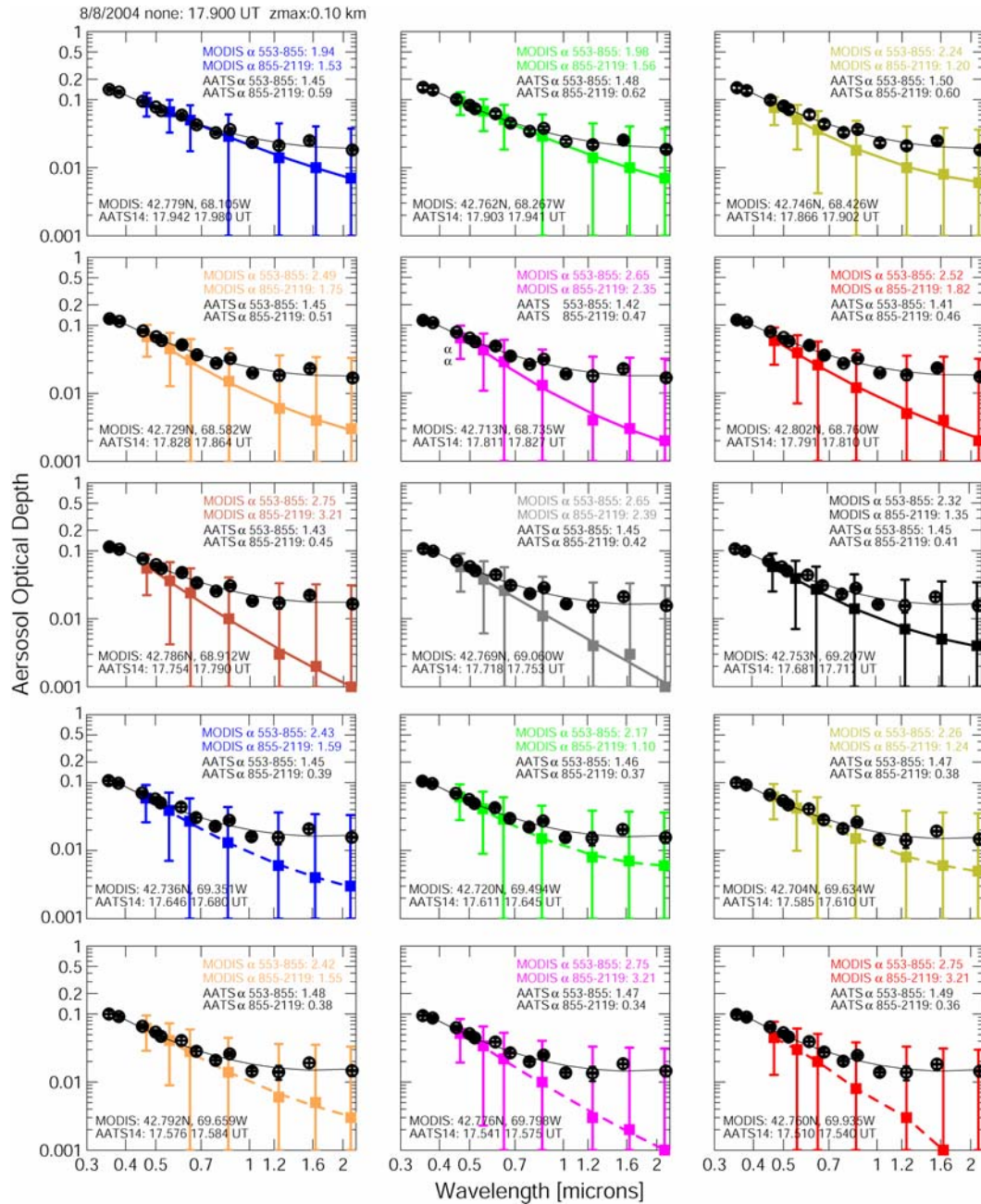


Figure 19. Comparison of AATS and MODIS AOD spectra and Ångström exponent values for 15 MODIS-Aqua grid cells of the 17.90 UT Aqua overpass on 8 August 2004.

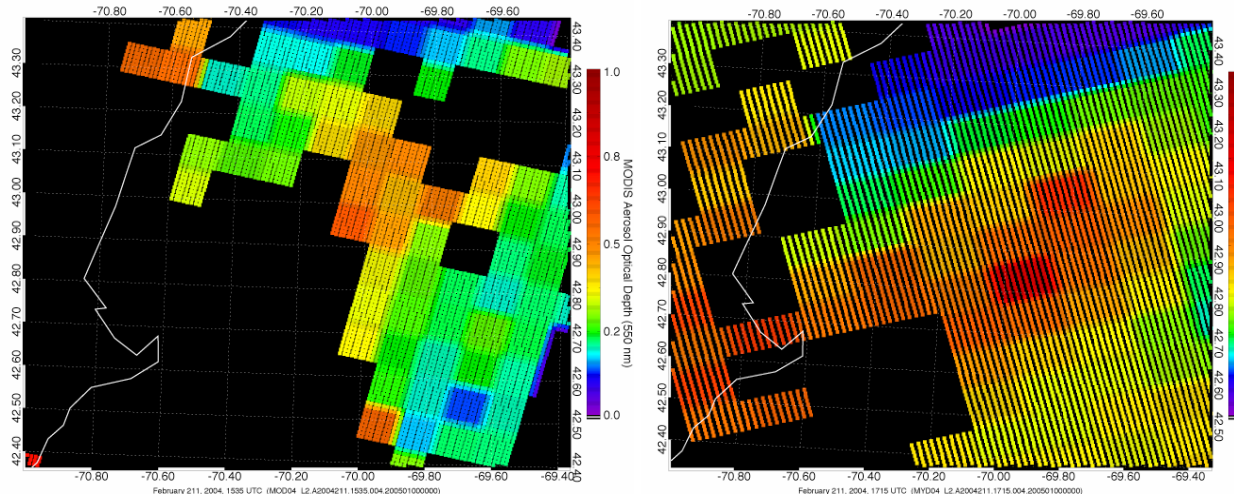


Figure 20. Fields of AOD retrieved from MODIS for 29 July 2004 with the glint mask reduced to 25°. **Left frame:** MODIS-Terra, 1535 UT. **Right frame:** MODIS-Aqua, 1715 UT.

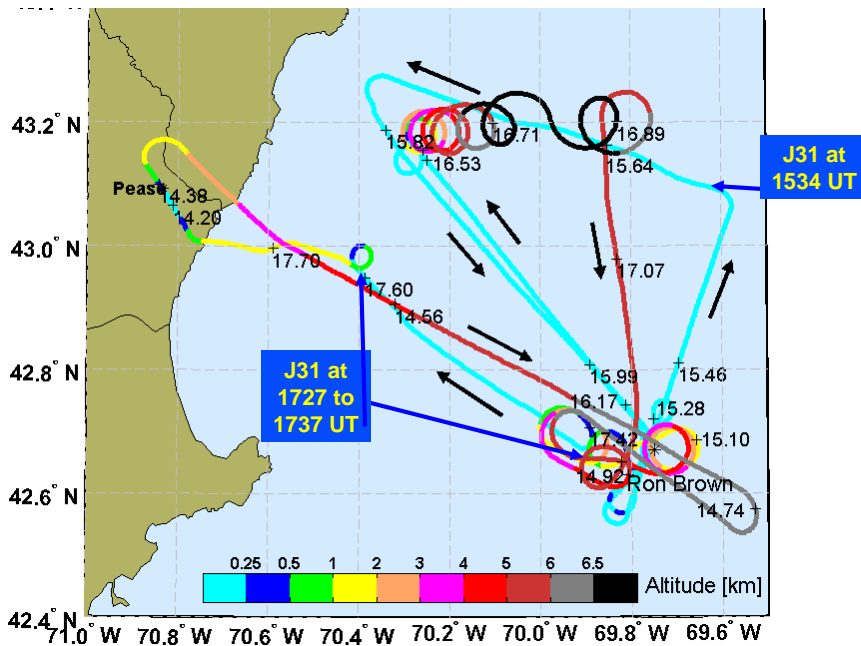


Figure 21. J31 flight path on 29 July 2004, underflying both Terra (1534 UT) and Aqua at or near minimum altitude (60 to 100 m).

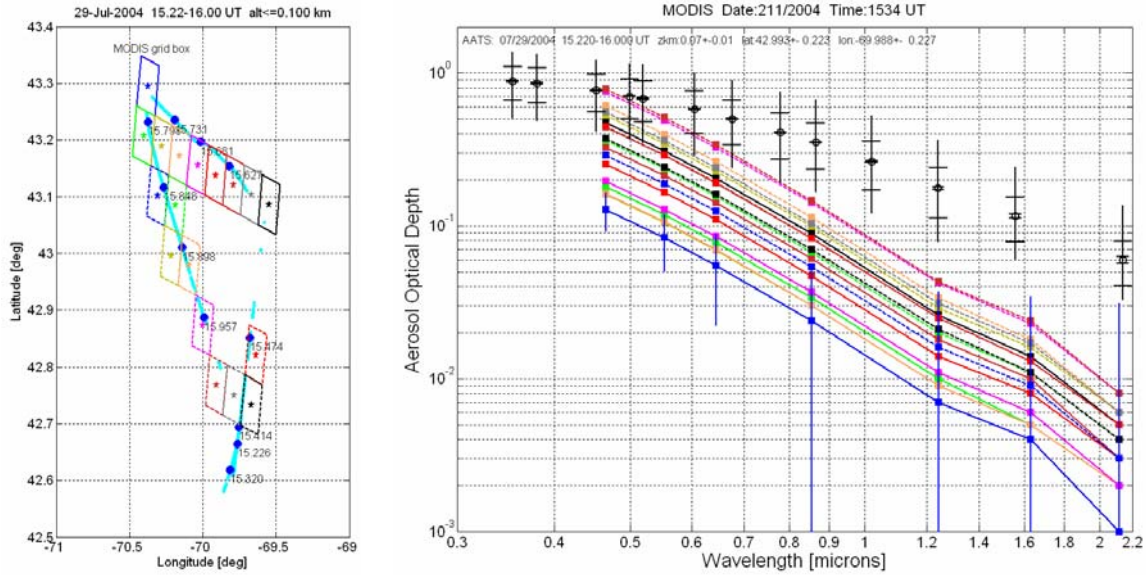


Figure 22. Comparison of AATS and MODIS-Terra AOD spectra for the 29 July 2004 1534 UT Terra overpass. Inset shows 16 MODIS grid cells that yielded AOD retrievals along the J31 low-altitude path. Resulting AOD spectra are color coded by grid cell color. The AATS spectrum (open black circles) is a mean from the whole low-altitude flight path shown, along with the typical AATS measurement uncertainty (narrow ticks), standard deviation of results along the flight path (wide ticks), and range along the flight path (vertical bars).

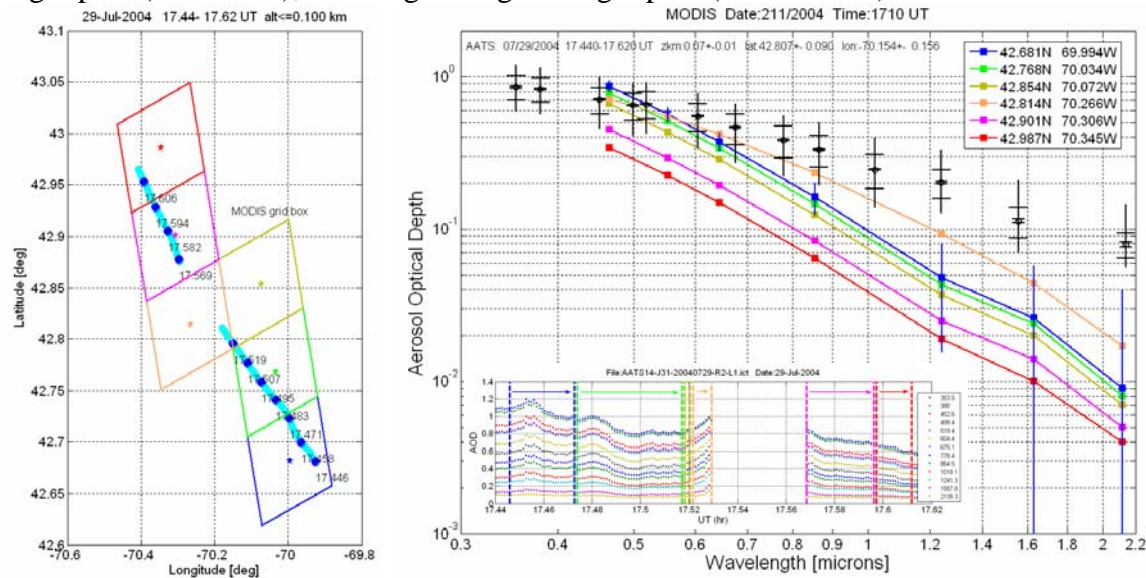


Figure 23. As in Figure 22, but for AATS and MODIS-Aqua AOD spectra for the 29 July 2004 1710 UT Aqua overpass, corresponding J31 low-altitude path, and 6 corresponding grid cells.